SYNTHESIS OF TRANSITION METAL COMPOUNDS FOR EFFICIENT ELECTROCATALYTIC WATER SPLITTING

HU Qingzhao

MPhil

The Hong Kong Polytechnic University

2019

The Hong Kong Polytechnic University

Department of Applied Physics

Synthesis of Transition Metal Compounds for Efficient Electrocatalytic Water Splitting

HU Qingzhao

A thesis submitted in partial fulfillment of the

requirements for the degree of Master of Philosophy

July 2018

CERTIFICATE OF ORIGINALITY

I hereby declare that this thesis is my own work and that, to the best of my knowledge and belief, it reproduces no material previously published or written, nor material that has been accepted for the award of any other degree or diploma, except where due acknowledgement has been made in the text.

_____ (Signed)

HU Qingzhao (Name of student)

Abstract

Electrochemical catalysts for the oxygen evolution reaction (OER) and hydrogen evolution reaction (HER) play a key role in highly-efficient water splitting and many other important energy conversion applications. Transition metal oxides are promising OER catalysts. In this work, Fe,W co-doped Co_3O_4 was grown on carbon fiber cloth ($FeWCo_3O_4$/CFC) and polypyrrole (PPy) coated carbon fiber cloth ($FeWCo_3O_4$/PPy/CFC) through a simple anodic electrodeposition method. The $FeWCo_3O_4$/CFC free-standing electrode reached an electrocatalytic current density of 30.7 mA cm^{-2} at 400 mV overpotential with a Tafel slope of 177 mV dec^{-1}. The PPy can serve as conductive binder to improve the contact between $FeWCo_3O_4$ and substrate. The resulting $FeWCo_3O_4$/PPy/CFC free-standing electrode reached an electrocatalytic current density of 36.2 mA cm^{-2} at 400 mV overpotential with a Tafel slope of 163 mV dec^{-1}. The $FeWCo_3O_4$/PPy/CFC free-standing electrode shows low electric resistance and is able to catalyze OER at 10 mA cm^{-2} for 12 hours without obvious decay under the optimized electrodeposition

conditions. This study provides new insight for design and synthesis of highly-efficient OER catalyst. Nickel sulfides synthesized via a simple one step hydrothermal method in this work exhibit superior HER catalytic performance. The nickel sulfide flakes grown on Ni plate substrate as free-standing electrode shows 112 mV overpotential to reach a current density of 10 mV cm^{-2} for HER. The nickel sulfides are mostly in a Ni_3S_2 form, which is found to be more catalytically active for HER than other nickel sulfides. EIS measurement indicates the small resistance of nickel sulfides. The nickel sulfides are highly stable under a current density of 10 mA cm^{-2} for 12 hours. OER and HER electrocatalysts are two crucial parts in electrochemical water splitting. This work is dedicated to improve the electrochemical water splitting efficiency by developing both OER and HER electrocatalysts.

List of Publications

1. **Qingzhao Hu**, Yan Liu, Longtao Ma, Xuming Zhang, Haitao Huang, PPy Enhanced Fe, W Co-doped Co_3O_4 Free-Standing Electrode for Highly-Efficient Oxygen Evolution Reaction. Journal of Applied Electrochemistry. https://doi.org/10.1007/s10800-018-1211-5

2. **Qingzhao Hu**, Yiran Ying , Yan Liu, Xuming Zhang, Haitao Huang, One Step Synthesis of Nickel Sulfides Flakes as Efficient Electrocatalyst for Hydrogen Evolution Reaction, under revision.

3. Longtao Ma, Huiqing Fan, Ke Fu, Shenhui Lei, **Qingzhao Hu**, Haitao Huang, Geping He, Protonation of Graphitic Carbon Nitride (g-C3N4) for an Electrostatically Self-Assembling Carbon@g-C3N4 Core–Shell Nanostructure toward High Hydrogen Evolution, ACS Sustainable Chemistry & Engineering, 2017, 5 (8), 7093–7103

Acknowledgments

Firstly, I would like to express my sincere appreciation to my chief supervisor Dr. Haitao Huang, for his continuous guidance and encouragement throughout my study period.

I would also like to thank my co-supervisor Dr. Xuming Zhang, for his help and support to my study.

I am happy to express my gratitude to Dr. Yan Liu, and Mr. Longtao Ma. They shared with me their valuable knowledge and provided precious advice on my research.

I am grateful to work with my groupmates Mr. Yiran Ying, Mr. Furong Qin, Dr. Ming Xu, Dr. Shu Zhu, Dr. Tao Li, Prof. Biaolin Peng, Dr. Guoge Zhang, Dr. Yuming Chen, and Dr. Xiaoyan Li.

I would like to appreciate the help and encouragement from my friends and colleagues Mr. Jin Liu, Mr. Yi Wang, Mr. Shi Zhao, Mr, Longxin Li, Dr. Linfeng Fei, Mr. Xing Li, Ms. Ruobing Song, Ms. Ting Wang, Ms. Yunfeng Wang, Dr. Mengye Wang, Ms. Feichi Zhou, Mr. Ziyuan Lin and Dr. Wei Lu.

Financial support from The Hong Kong Polytechnic University is also acknowledged.

Finally, I would like to express my highest thankfulness to my parents for all they give me.

Table of Contents

Abstract I

List of Publications III

Acknowledgments IV

Table of Contents VI

List of Figures VIII

List of Tables XI

Chapter 1 Introduction 1

1.1 Historical Background **1**

1.2 Research Objectives **12**

1.3 Fundamentals of Electrocatalysis **13**

1.3.1 Nernst Equation 14

1.3.2 Standard Hydrogen Electrode 18

1.3.3 Polarization of the electrode 20

1.3.4 Electrocatalytic Mechanism 22

1.4 Electrochemical Characterization **28**

1.4.1 Overall catalytic performance 28

1.4.2 Tafel Plot 29

1.4.3 Conductivity 29

1.4.4 Stability 30

1.5 Structure of Thesis **31**

Chapter 2 PPy Enhanced Fe, W Co-doped Co_3O_4 Free-Standing Electrode for Highly-Efficient Oxygen Evolution Reaction 33

2.1 Introduction **33**

2.2 Methods **37**

2.2.1 Electrodeposition 37

2.2.2 Fabrication of $FeWCo_3O_4$/CFC and $FeWCo_3O_4$/PPy/CFC 38

2.2.3 Characterization of $FeWCo_3O_4$/CFC and $FeWCo_3O_4$/PPy/CFC 41

2.3 Results and discussion **42**

2.4 Summary **58**

Chapter 3 One Step Synthesis of Nickel Sulfides Flakes as Efficient Electrocatalyst for Hydrogen Evolution Reaction 59

3.1 Introduction **59**

3.2 Methods **61**

3.2.1 Hydrothermal Method 61

3.2.2 Fabrication of Nickel Sulfides Flakes 61

3.2.3 Characterization of Nickel Sulfides Flakes 62

3.3 Results and Discussion **65**

3.4 Summary **80**

Chapter 4 Conclusions and Outlooks 81

4.1 Conclusions **81**

4.2 Outlooks **82**

References 84

List of Figures

Figure # ***Captions***

Figure 1.1 Shares of world primary energy sources

Figure 1.2 Schematic diagram of electrocatalytic water splitting.

Figure 1.3 Schematic diagram of standard hydrogen electrode.

Figure 1.4 Schematic diagram of influences of adsorbed intermediates on reaction activation energy

Figure 2.1 Schematic illustration of synthesis of $FeWCo_3O_4$/PPy/CFC

Figure 2.2 (a-c) SEM images of $FeWCo_3O_4$/CFC with different magnification,

Figure 2.3 (a-c) SEM images of $FeWCo_3O_4$/PPy/CFC with different magnification.

Figure 2.4 (a-c) TEM image, HRTEM image and corresponding SAED pattern of stripped $FeWCo_3O_4$ layer from $FeWCo_3O_4$/PPy/CFC.

Figure 2.5 (a) XRD pattern of electrodeposited $FeWCo_3O_4$/PPy/CFC. (b) Raman spectra of electrodeposited $FeWCo_3O_4$.

Figure 2.6 Measurements of (a) Co 2p XPS, (b) Fe 2p XPS, (c) W 4f XPS of $FeWCo_3O_4$/PPy/CFC.

Figure 2.7 (a) Polarization curve, (b) Tafel plot of $FeWCo_3O_4$/PPy/CFC and $FeWCo_3O_4$/CFC

Figure 2.8 (a) EIS plot and (b) Chronopotentiometric curve of $FeWCo_3O_4$/PPy/CFC and $FeWCo_3O_4$/CFC

Figure 2.9 EDS measurement of $FeWCo_3O_4$

Figure 2.10 Polarization curve of $FeWCo_3O_4$/PPY/CFC for 1 hour, 2 hour, 3 hour electrodeposition time.

Figure 2.11 Cyclic voltammetry curve of $FeWCo_3O_4$/CFC.

Figure 2.12 Cyclic voltammetry curve of $FeWCo_3O_4$/PPy/CFC.

Figure 3.1 (a) XRD pattern of nickel sulfides grown on nickel plates. (b) Raman shift curve of nickel sulfides grown on nickel plates.

Figure 3.2 (a) SEM image of nickel sulfides flakes with 5,000 magnification. (b) SEM image of nickel sulfides flakes with 10,000 magnification.

Figure 3.3 (a) TEM image of nickel sulfides flakes. (b) High resolution TEM image of nickel sulfides. (c) Selected area electron diffraction (SAED) pattern

of nickel sulfides.

Figure 3.4 (a) TEM image of nickel sulfides flakes. (b) High resolution TEM image of nickel sulfides. (c) Selected area electron diffraction (SAED) pattern of nickel sulfides.

Figure 3.5 (a) Polarization curve (b) Tafel plot.

Figure 3.6 (c) EIS plot (d) Chronopotentiometric curve of nickel sulfides.

Figure 3.7 (a), (b) Cyclic voltammetry of nickel sulfides grown on Ni plate under 2 mV/s scan rate.

Figure 3.8 Total and partial density of states (DOSs) for (a) NiS, (b) Ni_3S_2.

List of Tables

Table ***Captions***

Table 1. Summary of OER catalysts in the literature.

Table 2. Summary of HER catalyst in the literature.

Chapter 1 Introduction

1.1 Historical Background

The rapid development of technology has greatly improved the living conditions of human, accompanied by the accelerated global population growth in recent centuries. The current global human population is around 7 billion, while it is expected to grow into 9.3 billion in 2050 and 10.1 billion in 2100 with the current growth rate.[1] The world energy demand is also predicted to increase from the current 12billion ton oil equivalent (t.o.e) to 17 or 18 billion t.o.e. in 20 years. Carbon-dioxide emissions are forecasted to increase from 29 gigatons to 36-43 gigatons per year.[2] The speed of using fossil fuel is keeping on accelerating. Energy crises and global warming have raised word-wide attention to developing environmental-friendly energy sources. Climate change and other environmental issues require the usage of energy source to be sustainable and high efficiency.

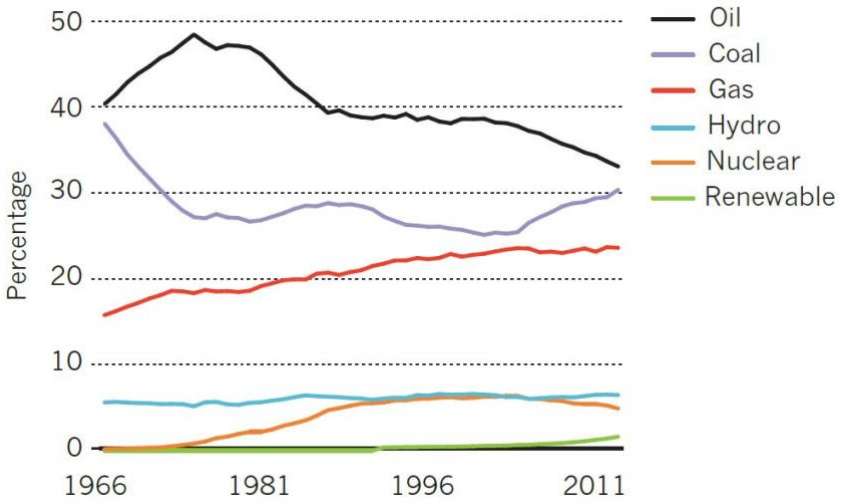

Figure 1.1 Shares of world primary energy sources.[2]

Fossil fuel currently dominates the energy supply as shown in Figure 1.1 Nuclear energy is increased in recent 30 years but still contributes only a small portion. To solve the energy crisis and challenge in climate change, a sustainable energy system that consists of production, conversion, delivery and consumption should be built. A sustainable fuel carrier is important to such sustainable energy system. Hydrogen that enjoys the advantages of free CO_2 emission and sustainability has potential to serve as sustainable fuel carrier.[3] To build a hydrogen energy system, problems regarding production, storing, delivery and consumption need to be solved. The production of hydrogen requires high energy conversion efficiency and environment friendliness. The current production of hydrogen in industry typically uses steam methane

reforming and coal gasification which involves severe CO_2 emission. To make the hydrogen production process free of CO_2 emission, huge efforts have been made in recent years, focusing on the investigation of hydrogen production from renewable energy sources. Researchers have been investigating the renewable energy derived hydrogen production by different methods, such as electrolysis, photolysis, biomass conversion.[4]

Electrolysis is a process that convert electricity into chemical energy. The CO_2 free hydrogen production can be realized through using electricity produced from renewable energy to electrolyze water into hydrogen and oxygen. This electrolysis process needs to exhibit high energy conversion efficiency to meet the requirement for commercial application. It should be reminded that hydrogen itself is not an energy source here but an energy carrier of sustainable energy sources such as solar energy, and wind energy. The motivation is that, when at low demand of electricity, the excess electric energy produced by solar or wind energies can be stored in hydrogen through electrocatalytic water splitting other than being wasted.

One of the key factors to increase electrolysis efficiency is to employ superior catalyst to reduce energy wasted at cathode side during hydrogen

evolution reaction (HER) and at anode side during oxygen evolution reaction (OER). Therefore, HER and OER catalysts for electrocatalytic water splitting have attracted ever-increasing research interests in recent years.

Electrocatalytic water splitting refers to the reaction: $2H_2O \rightarrow 2H_2 + O_2$ under applied voltage and catalysts. This reaction requires a minimum voltage of 1.23 V applied, which is derived from thermodynamic calculations. The two sub-reactions OER and HER happen at anode and cathode, respectively. In a typical water splitting reaction, the solution is acid or alkaline. In acidic solution, HER is considered to be

$$2H^+ + 2e^- \rightarrow H_2$$

and OER is considered to be

$$2H_2O \rightarrow O_2 + 4H^+ + 4e^-$$

In alkaline solution, HER is noted to be

$$2H_2O + 2e^- \rightarrow H_2 + 2OH^-$$

and OER is noted to be

$$4OH^- \rightarrow O_2 + 2H_2O + 4e^-$$

Excess voltage applied beyond the thermodynamic equilibrium voltage is called overpotential. Reversible hydrogen electrode (RHE) is often used as

reference electrode to calculate the overpotential. Zero voltage with respect to RHE is defined as the voltage that $2H^+ + 2e^- \leftrightarrow H_2$ reaches thermodynamic equilibrium. Therefore, the overpotential of HER is simply the excess voltage below zero voltage of RHE. The overpotential of OER is the excess voltage beyond 1.23 V with respect of RHE. OER is a four-electron transfer reaction which is considered to be very sluggish compared with the two-electron transfer HER. Thus huge efforts have been focused on developing OER catalysts.

There are two main approaches to increase the catalytic performance of HER and OER electrodes. One is to increase the intrinsic property of each catalytic site on the electrode. The other is to increase the total number of active sites on the electrode. To increase the intrinsic catalytic property, tuning surface adsorption energy of reaction intermediates can be adopted, which will be discussed in detail later. Various nanostructures can be used to increase the total number of active sites. The performance improvement by increasing total number of active sites is not as good as expected in theory due to transport limitations. The performance improvement by enhancing the intrinsic property keeps as good as expected in theory.[5]

OER catalysts contain a wide range of materials, typically noble-metal oxide (IrO_2, RuO_2)[6], earth-abundant transition metal oxides/ hydroxides/ nitrides/ borides/ sulfides /phosphides (NiFe Oxide[7], Co_3O_4[8], NiFe LDH[9], CoP[10]), carbon materials (g-C_3N_4[11]), and hybrid materials (NiFe LDH/rGO[12]). Single elements of nickel, cobalt and iron are researched intensively. The combination of Ni, Co, Fe are also reported by many studies. NiCoFe layered triple hydroxide (LTH) reported by Li et al. is the first time for LTH to be used as OER catalysts.[13] The NiCoFe LTH is grown on carbon fiber cloth (CFC) that is commonly used as electrode substrate due to its good conductivity, high specific surface area and flexibility. The NiCoFe LTH/CFC is fabricated simply through a 1.5 hour electrodeposition with CFC as the working electrode and Pt as the counter electrode at room temperature at 0.5 mA cm^{-2} reduction current density. The NiCoFe LTH/CFC shows excellent performance with 239 mV OER overpotential and 32 mV dec^{-1} Tafel slope. The favorable catalytic activity results from synergistic effect within Ni, Co, and Fe elements, efficient electron transfer and fast transportation of reaction species. Both intrinsic

catalytic property and active site numbers are considerably increased in this study.

Density functional theory (DFT) calculation is a powerful method in predicting material properties. The use of DFT in the study of gelled FeCoW oxyhydroxides helps the search for superior catalyst.[14] The optimal surface adsorption energies of reaction intermediates are key to catalytic performance. DFT calculations with Hubbard U (DFT+U) corrections indicate that the non-3*d* high valence metal tungsten can affect 3*d* metal oxides, such as FeCo oxides, to exhibit more favorable surface energetics to OER intermediates. The incorporation of W improves the intrinsic property of catalyst. The calculations compared the energetics of WO_3, CoOOH, FeOOH, $CoWO_4$, and Fe,W co-doped CoOOH. The optimal energetics are found in Fe,W co-doped β-CoOOH. A sol-gel method was adopted to synthesize FeCoW oxyhydroxide which is in a uniformly distributed amorphous structure with Fe:Co:W molar ratio of 1 : 1.02 : 0.70. The FeCoW oxyhydroxide catalyst needs only 191 mV overpotential to reach the 10 mA cm^{-2} OER current density when loaded on gold foam with 0.21 mg cm^{-2} mass loading in 1 M KOH without iR correction. The stability

of the catalyst is confirmed with no obvious catalytic activity decay for more than 500 hours. Substrate can also influence the catalytic overpotential required, which may be explained by electron transfer mechanism and available active sites. The overpotential is tested to be 315 mV on Au (111), 223 mV on glass carbon, and 191 mV on gold foam under a current density of 10 mA cm^{-2} in 1 M KOH. The gold foam used here is actually gold plated Ni foam. IR correction is a technique used to present intrinsic catalytic property by using overpotential measured minus the voltage drop on series resistance. The overpotential without iR correction is larger than that with the iR correction. Some studies adopt iR correction may hope to get rid of substrate resistance and fully focus on the catalytic property of the materials.

There are some advanced catalyst design techniques. Superlattice is an impressive design method. The superlattice of NiFe LDH nanosheet-graphene oxide (NiFe-GO) exhibits distinguished OER catalytic performance with 230 mV overpotential to reach 10 mA cm^{-2} and 42 mV dec^{-1} Tafel slope.[12] NiFe LDH is synthesized through a topochemical oxidation method.[15] NiFe LDH has a layered structure with positively charged NiFe hydroxide nanosheets and negatively charged anions exist in

between through electrostatic interaction. The bulk NiFe LDH can be exfoliated into NiFe LDH nanosheets and then assembled with graphene oxides to form superlattice hybrid. This superlattice structure of NiFe-GO benefits from high conductivity of GO and synergistic effect of alternatively stacked NiFe LDH sheets and GO.

Highly efficient HER catalysts attract huge research effort. Pt-based HER catalysts possess excellent HER catalytic performance, but they are very expensive which restricts their wide applications. Alternative HER catalyst materials are mostly metal sulfides (MoS_2[16], NiS[17]), metal selenides ($CoSe_2$[18]), metal phosphides (Ni_2P[19]) and metal nitrides (MoN[20]). Similar to OER catalysts, advanced HER catalysts can be synthesized through modifying the surface active site property and active site density. For example, MoS_2 grown on reduced graphene oxide (MoS_2/RGO) exhibit remarkable HER catalytic properties which result from large amount of active sites at MoS_2 nanoparticle edges and enhanced electron transportation along the RGO network.[16]

Despite of the huge effort that has been made on the research of electrochemical water splitting catalysts. There are still rooms for further improvement to meet the requirements for commercial application. The following tables summarize the performance of some of the OER and HER catalysts reported in recent literatures.

Table 1. Summary of OER catalysts in the literature.

OER Catalyst	Overpotential (mV) at 10 mA/cm^2	Tafel Slope (mV/dec)	Reference
NiCo ultrathin MOF nanosheet	189	42	[21]
FeCoW oxyhydroxide	191	37	[14]
$FeNi_3N$/NF	202	40	[22]
NiFe LDH-GO	230	42	[12]
CQD/NiFe LDH	235	30	[23]
NiCoFe LTH/CFC	239	32	[13]
NiFe LDH/CNT	247	31	[9]
De-$LiCo_{0.33}Ni_{0.33}Fe_{0.33}O_2$	295	35	[24]
Au@Co_3O_4	310	60	[25]
Graphene-Co_3O_4	313	56	[26]
CoMn LDH	324	43	[27]

NiP	344	49	[28]
CoP	345	47	[10]

Table 2. Summary of HER catalyst in the literature.

HER Catalyst	Overpotential (mV) at 10 mA/cm^2	Tafel Slope (mV/dec)	Reference
Ni_3S_2-rGO@NF	44	106	[29]
Fe-doped Ni_2P	84	73	[19]
Ni/Ni_3S_2	95	66	[30]
Co_9S_8-Ni_xS_y	163	88	[31]
MoS_2/rGO	150	41	[16]
NiS/NF	133	83	[17]
$CoSe_2$/CF	95	52	[18]
MoN	139	68	[20]

1.2 Research Objectives

The objectives of this research focus on the synthesis of cathode and anode materials that consist of earth-abundant elements with superb electrocatalytic performance. The anode and cathode are covered with catalysts as shown in Figure 1.2. When a voltage is applied, oxygen is formed at anode and hydrogen is formed at cathode. The reactions happen at the surface of anode and cathode. The present state-of-the-art catalysts are Pt for HER and IrO_2 for OER. However, the price and scarcity of Pt and Ir hinder their wide applications. The ideal catalyst should be able to catalyze HER or OER to reach higher current density with lower voltage required and synthesized with earth-abundant elements.

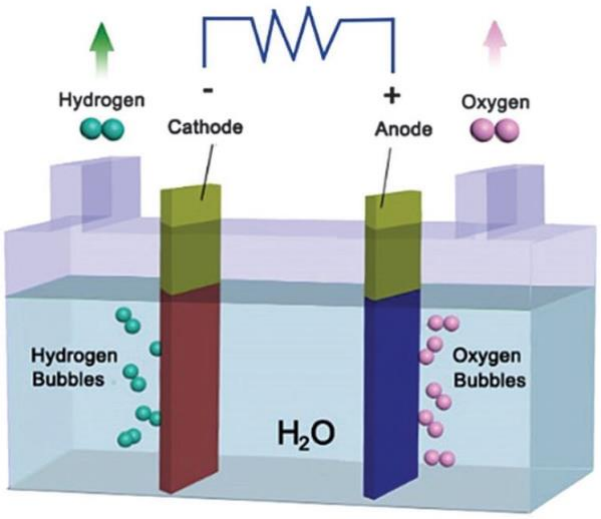

Figure 1.2 Schematic diagram of electrocatalytic water splitting.[4]

The parameters to describe the performance of OER and HER catalysts include overpotential, Tafel slope, conductivity, and stability. Overpotential is the excess voltage needed to reach specific current density. Tafel slope reveals the catalytic mechanism and is related to the intrinsic catalytic activity. Conductivity shows the resistance of the material to transfer electrons between electrolyte and electrode. Stability refers to the chemical stability when the voltage is applied and mechanical stability when oxygen or hydrogen bubbles come out of the electrolyte. Improvement of these parameters are the objectives of the research.

1.3 Fundamentals of Electrocatalysis

Electrocatalysis is basically a combination of electrochemistry and catalysis. The underling knowledge consists of physical chemistry. Principles in physics can be helpful to the understanding of the reaction process at the electrode. The interface between cathode/anode and electrolyte can be well described by thermodynamics.

Electrochemistry focuses on the investigation of conversion between electric energy and chemical one, typically involving reactions occurred within the

electrode and electrolyte. The electron or charge transfer at the interface between electrode and electrolyte is the key to electrochemistry. For example, in HER, hydrogen ions move towards the cathode and combine with electrons to form hydrogen atom adsorbed on the surface of cathode, which will finally form hydrogen gas through desorption.

1.3.1 Nernst Equation

Nernst equation is used to calculate the relative potential to standard hydrogen electrode when the reaction between oxidation and reduction reaches an equilibrium.

For a general electrode reaction:

$$\mathrm{Ox} + \mathrm{n}e^{-} \leftrightarrow \mathrm{Red}$$

where Ox represents oxidation state, Red represents reduction state.

Then the Nernst equation writes:

$$\varphi = \varphi^{0} + \frac{RT}{nF} ln \frac{a_{ox}}{a_{red}}$$

where φ is the potential.

φ^{0} is the standard hydrogen electrode potential.

R is the universal gas constant.

T is the absolute temperature.

n is the number of electrons transferred.

F is the Faraday constant.

a_{ox} is the activity of oxidation state.

a_{red} is the activity of reduction state.

For example, at 25 ℃, T = 298 K, R = 8.314 J K^{-1} mol^{-1}, F = 96485 K mol^{-1}.

$$\varphi = \varphi^0 + \frac{0.0591}{n} log \frac{a_{ox}}{a_{red}}$$

a_{ox} and a_{red} usually adopt the average concentration.

For a more general form of reaction:

$$aA + bB \leftrightarrow cC + dD$$

where A, B, C, and D represent reaction chemicals. a, b, c, and d represent the amounts of the corresponding reaction chemicals.

From the thermodynamics of equilibrium, the equilibrium constant writes:

$$K_{eq} = \frac{[C]_{eq}^{c}[D]_{eq}^{d}}{[A]_{eq}^{a}[B]_{eq}^{b}}$$

where K_{eq} is the constant for a reaction. If the reaction is not at equilibrium, the number

$$Q = \frac{[C]^{c}[D]^{d}}{[A]^{a}[B]^{b}}$$

will not be equal to K_{eq}. If Q $<$ K_{eq}, the reaction will shift towards the right, which means more C and D will be formed. If Q $>$ K_{eq}, the reaction will shift towards the left, which means more A and B will be formed. If Q = K_{eq}, the reaction reaches an equilibrium.

The change of Gibbs free energy for a reaction is:

$$\Delta G = \Delta G^0 + RTlnQ$$

where ΔG^0 is the change of Gibbs free energy for the reaction under standard condition, which means 1 M concentration for dissolved spices and 1 atm pressure.

$$\Delta G^0 = -RTlnK_{eq}$$

So when the reaction is in equilibrium, Q=K_{eq}, then

$$\Delta G = \Delta G^0 + RTlnQ$$

$$= -RTlnK_{eq} + RTlnQ \quad = 0$$

It means that, when the reaction reaches equilibrium, the change of Gibbs free energy of reaction becomes zero.

In electrochemistry,

$$\Delta G = -nFE$$

where n is the number of electrons transferred.

F is the Faraday constant.

E is the electromotive force.

Under standard condition,

$$\Delta G^0 = -nFE^0$$

So ,

$$-nFE = -nFE^0 + RTlnQ$$

This equation can also be written as:

$$\mathrm{E} = E^0 - \frac{RT}{nF} lnQ$$

This equation is the Nernst equation in a more general form.

The total reaction for water splitting with 4 electrons transferred is:

$$2H_2O \rightarrow 2H_2 + O_2$$

The change of Gibbs free energy is calculated to be 474380 J.

$$E = -\frac{4F}{\Delta G}$$

$$= -1.23\ V$$

So the theoretical least voltage for water splitting can be derived as 1.23 V.

1.3.2 Standard Hydrogen Electrode

The absolute potential of one electrode is difficult to measure. In practice, reference electrode such as standard hydrogen electrode is usually used. A relative potential is expressed with respect to the standard hydrogen electrode.

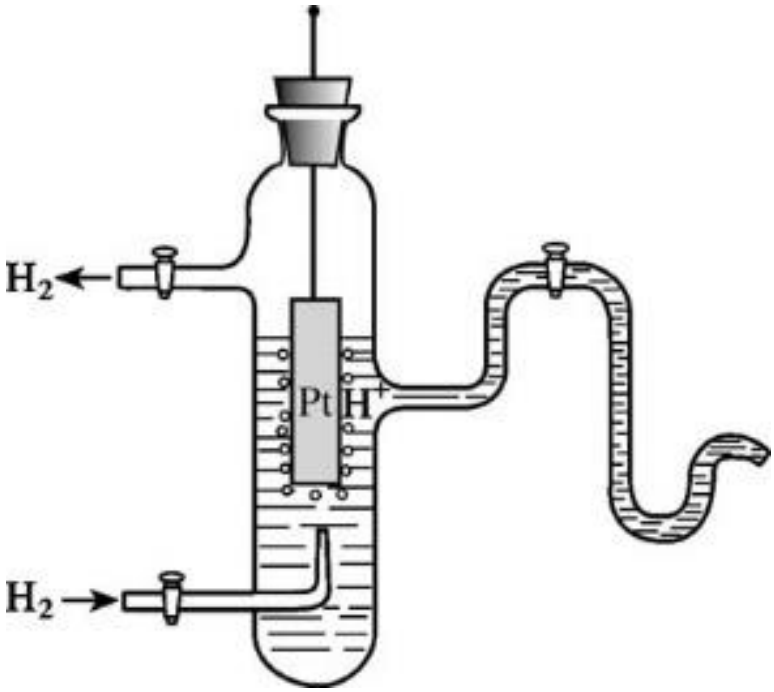

Figure 1.3 Schematic diagram of standard hydrogen electrode.

Standard hydrogen electrode is usually a Pt electrode immersed in an idea acidic solution when equilibrium is reached, where hydrogen gas is under 100 kPa, activity of hydrogen ions is 1 M. As shown in Figure 1.3, in a typical standard hydrogen electrode, the hydrogen is under 1 bar pressure in 0.5 mol/L

H_2SO_4 solution. Hydrogen gas is bubbled into the solution continuously. Hydrogen gas can be adsorbed at the surface of Pt plate. The adsorbed hydrogen gas may lose electron and be oxidized into hydrogen ions. Hydrogen ions in the solution may acquire electron and be reduced into hydrogen gas. The following reversible reaction occurs:

$$H_2 \leftrightarrow 2H^+ + 2e^-$$

The adsorbed hydrogen gas is actually the electrode called standard hydrogen electrode. The Pt plate is just the carrier and conductive substrate for hydrogen. The potential difference between standard hydrogen electrode and solution is called standard hydrogen electrode potential and defined as zero with respect to the standard hydrogen electrode. The absolute value is 4.44 ± 0.02 V at 25 ℃.

Reversible hydrogen electrode is a hydrogen electrode that does not have the requirement on activity of hydrogen ions. So the reversible hydrogen electrode potential varies with the pH of the solution. From the Nernst equation,

$$\varphi = \varphi^0 + \frac{RT}{F} ln \frac{a_{H^+}}{\sqrt{\frac{p_{H_2}}{p_0}}}$$

where a_{H^+} is the activity of hydrogen ions.

p_{H_2} is the pressure of hydrogen gas.

p_0 is the standard pressure.

Take 25 ℃ into calculation:

$$\varphi = -0.059\, pH$$

Reversible hydrogen electrode is commonly used in electrocatalytic water splitting, since there is no need to adjust the overpotential when measured in solutions that under different pH values.

1.3.3 Polarization of the electrode

Polarization of the electrode implies that the potential of the electrode has changed from the equilibrium potential due to the current transported through the electrode. The equilibrium electrode potential noted as φ_e is the potential without current flowing through. The polarization at the anode is called anodic polarization which makes the anode potential more positive. The polarization at the cathode is called cathodic polarization which makes the cathode potential more negative. The electrode potential will be more polarized as the current density flowing through the electrode is increased. The difference between electrode potential and equilibrium electrode potential is defined as overpotential.

$$\Delta\varphi = \varphi - \varphi_e$$

The overpotential is $\Delta\varphi > 0$ for anodic polarization. The overpotential is $\Delta\varphi < 0$ for cathodic polarization.

For electrode reaction such as:

$$\mathrm{Ox} + e^{-} \leftrightarrow Red$$

Ox is in oxidation state. Red is in reduction state. At equilibrium condition, $\Delta\varphi = 0$, the oxidation reaction rate $i^{\rightarrow}$ equals to the reduction reaction rate $i^{\leftarrow}$

$$i^{\rightarrow} = i^{\leftarrow} = i_0$$

where from electrochemical kinetics,

$$i^{\rightarrow} = FK_1C_{Ox}e^{-\beta F\varphi_e/RT}$$

$$i^{\leftarrow} = FK_2C_{Red}e^{(1-\beta)F\varphi_e/RT}$$

Thus the exchange current density i_0 is the solution of

$$FK_1C_{Ox}e^{-\beta F\varphi_e/RT} = FK_2C_{Red}e^{(1-\beta)F\varphi_e/RT}$$

where F is the Faraday constant.

K_1 is the reduction rate constant.

K_2 is the oxidation rate constant.

C_{Ox} is the concentration of the oxidation state species.

C_{Red} is the concentration of the reduction state species.

β is the constant that reflects the influence of electrode potential on reaction Gibbs free energy.

When the electrode is no longer at the equilibrium potential,

$$i^{\rightarrow} \neq i^{\leftarrow}$$

Polarization current *i* occurs,

$$i = i^{\rightarrow} - i^{\leftarrow}$$

The polarization current depends on the polarization potential. From Butler-Volmer formula:

$$i = i_0\left(e^{-\beta F\Delta\varphi/RT} - e^{(1-\beta)F\Delta\varphi/RT}\right)$$

At high overpotential, this equation can be simplified as:

$$\Delta\varphi = a + b\ log i$$

Thus we can conclude that *log*i linearly depends on the overpotential $\Delta\varphi$.

1.3.4 Electrocatalytic Mechanism

Electrocatalysis is defined as the phenomenon that the electrode reaction is significantly changed while the electrode remains unchanged. The materials that can perform electrocatalysis are called electrocatalysts. The electrocatalyst can be the electrode itself and can also be coated on the surface of the electrode. Species in the electrolyte often have obvious influences on the electrocatalysis,

such as reducing the Faraday efficiency. When the same electrode reaction occurs on different electrode surfaces, generally, the electrode that requires less overpotential to reach a certain current density possesses higher electrocatalytic performance. This means that higher exchange current density i_0 indicates higher electrocatalytic performance. However, Tafel slope is also important, especially at high overpotential. For electrode with small i_0, high current density can also be achieved at high overpotential if Tafel slope is sufficiently small.

The overall electrocatalytic performance is mainly determined by two aspects. The first one is the morphology. Large specific surface area leads to more available active sites. The second one is the reaction energetics. The process in which catalysts interact with the reaction intermediates and reaction products will directly change the reaction activation energy.

OER is a four electron transfer reaction with three reaction intermediates as HOM, OM, HOOM. The M represents an active site for adsorption on the catalyst surface. HER is a two electron transfer reaction with one reaction intermediate HM. The OER reaction can be described as following:

$$H_2O \rightarrow HOM + H^+ + e^-$$

$$\mathrm{HOM} \rightarrow OM + H^+ + e^-$$

$$OM + H_2O \rightarrow HOOM + H^+ + e^-$$

$$\mathrm{HOOM} \rightarrow O_2 + H^+ + e^-$$

The HER reaction can be noted as following:

$$H^+ + e^- \rightarrow HM$$

$$H^+ + HM + e^- \rightarrow H_2$$

The reaction intermediates are adsorbed on the surface active sites. The bond strength reflects the binding energy between intermediates and active sites and determines the catalytic property according to Sabatier principle, which is a well-accepted theory to describe OER and HER catalytic mechanisms.[32]. It has been found that the binding energies between OER reaction intermediates OH, O, HOO and surface active sites are linearly correlated.[33] It means that the active site that bonds OH stronger than other active sites will also bonds O and HOO stronger than other active sites. The optimal catalyst surface active sites should bind reaction intermediates neither too strong nor too weak. Weak binding will lead to difficulty in reaction activation. Strong binding will suffer from hardship in release of reaction products. For HER, surface active sites with the optimal H binding energy will enjoy the best HER catalytic

performance. Pt with superior HER catalytic property is shown to possess favorable H binding energy.[34] For OER, there are so-called scaling relationship between the intermediates OH and HOO, as their binding energy difference on active sites is always 3.2 ± 0.2 eV. The optimum difference is 2.46 eV. Therefore, theoretically, the best OER catalyst is difficult to reach.[35] According to Sabatier principle and scaling relationship, catalysts whose binding energies are the closest to the optimum values will show the best catalytic properties.

The electrocatalytic process in HER mainly involves the adsorption and desorption of hydrogen on the electrode surface, which is often noted as M-H where M is the surface active site. The adsorption and desorption processes of hydrogen on different materials are different. The hydrogen evolution rates differ tremendously on different electrode materials at certain overpotential. This is resulted from the different reaction energetics for hydrogen adsorption and desorption.

It is observed that the exchange current density i_0 increases with increasing M-H adsorption energy for some metals with high HER onset overpotentials, such as Hg and Zn. These metals have weak adsorption for hydrogen. Therefore, the adsorption of hydrogen is the process to control the overall hydrogen evolution rate. Increase of the hydrogen adsorption energy will sufficiently increase overall hydrogen evolution rate. For metals with high adsorption energy, such as Fe and Ni. The reaction rate is controlled by hydrogen desorption process. The increase of adsorption energy will otherwise harm the evolution rate of hydrogen. The different processes are shown in Figure 1.4. For adsorption process, the activation energy needed is E_a for hydrogen adsorption to form M-H. The activation energy needed for hydrogen evolution is E_b. The change of M-H adsorption energy will lead to different activation energies E'_a for hydrogen adsorption and E'_b for hydrogen evolution. The decrease of activation energy from E_a to E'_a will not lead to overall increase of hydrogen evolution rates since the desorption activation energy has increased from E_b to E'_b. The overall hydrogen evolution rate is now controlled by desorption process. Therefore, the optimal surface reaction energetics can be reached under a balance of all sub-reaction processes.

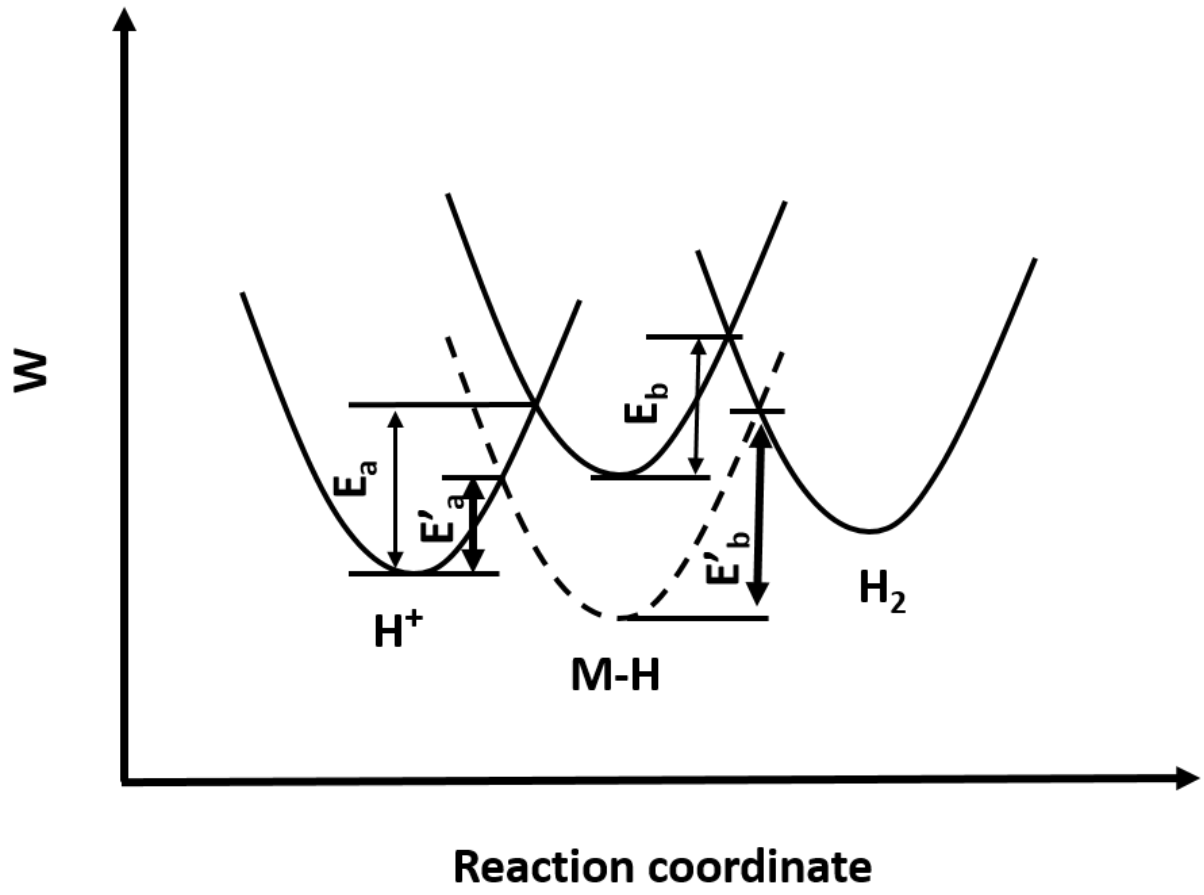

Figure 1.4 Schematic diagram showing the influences of adsorbed intermediates on reaction activation energies.

1.4 Electrochemical Characterization

1.4.1 Overall catalytic performance

The overall catalytic performance is usually measured using cyclic voltammetry (CV) or linear sweep voltammetry (LSV). The current density is measured under different voltages. The actual voltage applied on the water splitting cell is

$$U = U_0 + \eta_a + \eta_c + IR$$

where U_0 is the theoretical voltage which is 1.23 V for water splitting.

η_a is the overpotential at anode.

η_c is the overpotential at cathode.

IR is the total voltage drop for current flow.

Considering that the non-faradaic capacitance will contribute to the total current, small scan rate should be adopted to minimize the current resulted from other processes. The total current measured is actually the sum of non-faradaic capacitance, surface reaction species and water splitting current. CV and LSV provide the overall performance of the electrode. Factors as exchange current density, Tafel slope, specific surface area and total resistance are all reflected in this measurement.

1.4.2 Tafel Plot

Tafel plot is the diagram describing the overpotential as a function of log i. The mathematical expression for the current is,

$$i = i_0(e^{-\beta F\Delta\varphi/RT} - e^{(1-\beta)F\Delta\varphi/RT})$$

In practice, at high overpotential region, the overpotential has a linear relationship with log i.

$$\Delta\varphi = a + b\ logi$$

The parameter b is defined as Tafel slope. Tafel slope reflects the reaction energetics of the electrocatalytic processes. Small tafel slope indicates favorable catalytic energetics.

1.4.3Conductivity

Conductivity is usually reflected in the electrochemical impedance spectroscopy (EIS) measurement. A small sinusoidal voltage signal is applied on the electrode and the current is measured. The sinusoidal signal varies from low frequency to high one. The signal amplitude is small which will not affect the electrode equilibrium state. The resistance will directly influence the

voltage drop through the water splitting cell. Low conductivity will suffer from inefficient energy waste. The sinusoidal voltage signal can be expressed as,

$$E(t) = E_0 \cos(\omega t)$$

The current generated is,

$$I(t) = I_0 \cos(\omega t - \varphi)$$

The impedance is thus calculated as,

$$Z(t) = \frac{E(t)}{I(t)}$$

$$Z(t) = Z_0 \frac{\cos(\omega t)}{\cos(\omega t - \varphi)}$$

For different frequency ω,

$$Z(\omega) = Z_0(cos\phi + jsin\phi)$$

The plot in which the real part of impedance is plotted as *x*-axis and the imaginary part is plotted as *y*-axis is called Nyquist plot. In a Nyquist plot, the length of vector is the impedance and the angle between vector and *x*-axis is the phase shift ϕ.

1.4.4 Stability

The stability implies both the electrochemical stability and mechanical one. The electrochemical measurement is conducted in 1 M KOH solution. The electrode materials should be stable in strong alkaline environment. At high

overpotential, hydrogen or oxygen bubbles may affect the mechanical structures of the electrocatalysts. High stability is expected to conduct 10 mA cm^{-2} without obvious performance decay for a certain period, 12 hours for example.

1.5 Structure of Thesis

The chapters of this thesis are organized as follows:

Chapter 1: The background knowledge is introduced in details. The historical background explains the situation of energy demand for human beings. Current research hot topics are also involved. Then the objective of this work is explained. To develop highly efficient electrocatalyst, fundamental knowledge is reviewed. The parameters to characterize electrocatalyst are explained in the electrochemical characterization part.

Chapter 2: The work of PPy enhanced Fe, W co-doped Co_3O_4 free-standing electrode is showed in details. The introduction part gives the explanations of the development of OER electrochemical catalysts. The design strategies of

this high performance electrode are discussed. The method part firstly introduces the fundamental background of electrodeposition and then shows the experimental details of fabrication and characterization. Results and discussion are explained, followed by a short summary.

Chapter 3: Nickel sulfide flakes as high efficient HER electrocatalyst are synthesized by a hydrothermal method. Fabrication and characterization details are shown. The HER catalytic performance is investigated and the results are discussed. DFT calculations are performed to explain the marvelous property of the synthesized nickel sulfides. A short summary is also given.

Chapter 4: The conclusions of the whole thesis are summarized. Outlook for future work is briefly discussed.

Chapter 2 PPy Enhanced Fe, W Co-doped Co_3O_4 Free-Standing Electrode for Highly-Efficient Oxygen Evolution Reaction

2.1 Introduction

Energy crisis and global warming have raised worldwide interest in developing environmental friendly energy sources [2, 3, 36]. Alternatives to fossil fuels are significant to help reduce green-house effect and air pollution [36, 37]. Hydrogen, which is recognized as a clean and renewable energy source, possesses great potential to become the next generation energy source [3, 36]. Hydrogen production through methane or coal in industry involves enormous carbon dioxide emission [4]. While mass production of hydrogen by electrolysis with high efficiency remains laborious due to the sluggish kinetics of oxygen evolution reaction (OER) in water splitting [4, 38]. Superb catalyst which can promote the oxygen evolution is crucial to the production of hydrogen through water splitting. The state-of-the-art catalysts RuO_2 and IrO_2 suffer from high cost and low abundance [39]. Catalyst fabricated with earth-

abundant elements is therefore needed to surmount the reaction obstacles and increase the efficiency.

Recent years have seen huge efforts made on the synthesis of transition metal-based materials [5, 12, 14, 24, 40-43], such as transition metal oxides and transition metal (oxy)hydroxides (CoOOH [44], NiCoFe layered triple hydroxide [13], FeCoW oxyhydroxide [14]), transition metal phosphides (CoP [10], NiP [28]), metal-organic frameworks (NiCo bimetal-organic framework [21]) and composites (NiFe layered double hydroxide-graphene oxide [12]). Some OER catalysts derived from Co_3O_4 have been reported, such as Au@Co_3O_4 core-shell nanocrystals [25] and graphene-Co_3O_4 nanocomposite [26]. However, the synthesis of Au@Co_3O_4 core-shell nanocrystals involves noble metal, which is adverse to industry application. The synthesis method of graphene-Co_3O_4 nanocomposite is complicated and high temperature calcination is also required. In addition, binder such as Nafion is needed for powder catalysts to fabricate electrodes [21, 45]. Therefore, the fabrication of free-standing electrode with highly-efficient OER catalysts that consist of earth-abundant elements is attractive and challenging.

There are two general approaches to the development of an effective catalyst: improving the intrinsic property of each site or increasing the amount of

effective sites. Intrinsic property can be enhanced by tuning binding energies of reaction intermediates. Morphology design contributes to the number of effective active sites [5]. A recent study predicted the superior intrinsic catalytic performance of FeCoW oxyhydroxide by calculating the corresponding binding energies of the intermediates using density functional theory (DFT+U) [14]. Non-3d high-valence metals such as tungsten can modulate 3d metal oxides to provide more optimal adsorption energies and electronic structure for highly efficient OER. Cobalt-based composites supported on carbon fiber substrate are investigated to be highly-efficient electrochemical catalysts, which may result from high electric conductivity and synergistic effect between cobalt oxide/cobalt and carbon substrate.[46, 47] It is reported that PPy/carbon structure can increase the metal availability for electrode reaction.[48] Meanwhile, PPy can form Co-N active sites with cobalt to possess enhanced electrochemical property.[49, 50] Therefore, a highly-efficient OER catalytic electrode is expected through the fabrication of FeCoW catalyst supported by PPy/CFC substrate.

Herein, $FeWCo_3O_4$/PPy/CFC free-standing electrode was synthesized through a simple electrodeposition method and showed efficient OER catalytic

performance. The electrochemical results demonstrated that the $FeWCo_3O_4$/PPy/CFC electrodes achieved a higher current density of 36.2 mA cm^{-2} than $FeWCo_3O_4$/CFC (30.7 mA cm^{-2}) at an overpotential of 400 mV. The PPy can improve the contact of active material with substrate, which enables better OER electrocatalytic performance of $FeWCo_3O_4$/PPy/CFC electrode than $FeWCo_3O_4$/CFC electrode.

2.2 Methods

2.2.1 Electrodeposition

Electrodeposition is a facile method to grow materials on the electrode. In terms of electrode reaction, electrodeposition can be classified into Faradaic and non-Faradaic processes. In Faradaic process, charges move across the electrode-solution interface, such as cathodic coating of metal. Metal ions receive electrons from the cathode and are reduced into metal. The metal is coated and deposited on the cathode. In non-faradaic process, no charges move across the electrode-solution interface. Charged species are attracted to the electrode with the opposite charge. The concentration change of species at the electrode surface will lead to the deposition of non-faradaic process. Anodic deposition of Co_3O_4 is studied by many researchers. According to anodic deposition with tartrate (tart) in the solution[51], the Co^{2+} can be firstly oxidized into Co^{3+} and then be deposited as Co_3O_4 through the following reaction:

$$2Co^{2+}(tart) \rightleftharpoons 2Co^{3+} + 2(tart) + 2e^-$$

$$2Co^{3+} + Co^{2+}(tart) + 8OH^- \longrightarrow Co_3O_4 + (tart) + 4H_2O$$

The growth of Co_3O_4 deposited on the anode involves both faradaic and non-faradaic processes. The anodic deposition of Co_3O_4 is also studied by Casella.[52] In the electrodeposition solution, Co^{2+} may exist in a dimeric complex species with Gluconate ion (L^{3-}) as $Co_2L_2^{2-}$. The anodic deposition may occur as the following equation:

$$3Co_2L_2^{2-} + 16OH^- \longrightarrow 2Co_3O_4 + 6L^{3-} + 8H_2O + 4e^-$$

The addition of Trisodium citrate dehydrate in the solution can also lead to the formation of negatively charged complex species with Co^{2+} ions and Fe^{2+} ones. These negatively charged species will move towards anode and participate in anodic deposition.

2.2.2 Fabrication of $FeWCo_3O_4$/CFC and $FeWCo_3O_4$/PPy/CFC

Preparation of carbon fiber clothes

Carbon fiber cloth (CFC) was firstly washed with deionized water (DI water) and acetone several times, then immersed into dilute nitric acid for 24 hours to remove surface impurities. Thereafter, the CFC was washed with DI water and dried at 60 ℃ in oven for 2 hours for further use.

PPy grown on CFC (PPy/CFC)

Pyrrole (1 mL) was firstly dissolved into DI water (50 mL). Then ammonium persulfate (1 g) and sodium p-toluenesulfonate (1 g) were added into the above solution. Thereafter, the solution was placed into ice bath and stirred for 10 mins. CFC was put into the solution for polymerization for 2 hours to obtain PPy/CFC. The PPy/CFC was washed with DI water several times and dried at 60 ℃ in oven for 2 hours.

Fe, W doped Co_3O_4 grown on PPy/CFC ($FeWCo_3O_4$/PPy/CFC)

The electrodeposition parameters were adopted from the research work by Stojek [53]. Trisodium citrate dehydrate (14.75 g), boric acid (2.56 g), sodium tungstate (19.5 g), Iron(II) chloride tetrahydrate (0.49 g) and cobalt chloride hexahydrate (0.59 g) were dissolved into DI water (250 mL). Phosphoric acid (1.9 mL, 85 wt%) was added into the above solution. Then the solution was put under ultrasonic condition for 1 hour. After that, the solution was stirred for 12 hours to become homogenous. The above solution was then added into an electrochemical cell with PPy/CFC as anode and Pt plate as cathode. Electrodeposition was conducted under a constant current of 40 mA cm^{-2} for 2

hours at 60 ℃. The deposited $FeWCo_3O_4$/PPy/CFC was washed with DI water and ethanol for several times.

Fe, W doped Co_3O_4 grown on CFC ($FeWCo_3O_4$/CFC)

Trisodium citrate dehydrate (14.75 g), boric acid (2.56 g), sodium tungstate (19.5 g), Iron(II) chloride tetrahydrate (0.49 g) and cobalt chloride hexahydrate (0.59 g) were dissolved into DI water (250 mL). Phosphoric acid (1.9 mL, 85 wt%) was added into the above solution. Then the solution was put under ultrasonic condition for 1 hour. After that, the solution was stirred for 12 hours to become homogenous. The above solution was added into an electrochemical cell with CFC as anode and Pt plate as cathode. Electrodeposition was conducted under a constant current of 40 mA cm^{-2} for 2 hours at 60 ℃. The deposited $FeWCo_3O_4$/CFC was washed with DI water and ethanol for several times.

2.2.3 Characterization of $FeWCo_3O_4$/CFC and $FeWCo_3O_4$/PPy/CFC

Scanning electron microscope (SEM, TM 3000, Hetachi, Janpan) and Transmission electron microscope (TEM, JOEL JEM-2010, Janpan) were used for microstructure and morphology characterization. X-ray diffraction (XRD, Rigaku D/max ⅢA, Cu Kα, λ=0.15418 nm, Japan) was used for crystalline structure analysis. Raman spectrum was conducted on a HORIBA Raman spectrometer at 488 nm. X-ray photoelectron spectroscopy (XPS, Thermo Microlab 350) was used to study the surface composition of $FeWCo_3O_4$ inside an ultrahigh vacuum system.

Electrochemical Measurement

Linear sweep voltammetry (LSV), cyclic voltammetry (CV), electrochemical impedance spectroscopy (EIS, 0.01-1000k Hz frequency) and chronopotentiometric tests were performed on electrochemical workstation (Solartron Analytical 1470E). A classical three-electrode configuration was used with Pt plate as counter electrode and saturated calomel electrode (SCE) as reference electrode. The measurement was conducted in 1 mol L^{-1} KOH solution and the polarization curve was tested at a scan rate of 2 mV s^{-1}.

2.3 Results and discussion

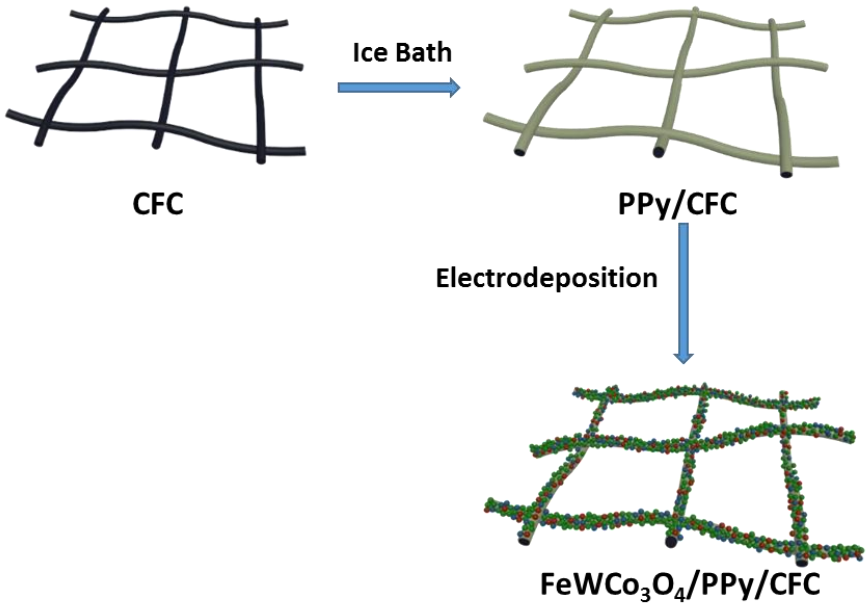

Figure 2.1 Schematic illustration of synthesis of $FeWCo_3O_4$/PPy/CFC.

The CFC is firstly covered with a thin layer of PPy in an ice bath as shown in Figure 2.1 The Fe, W doped Co_3O_4 is grown on the surface of PPy through a simple electrodeposition afterwards.

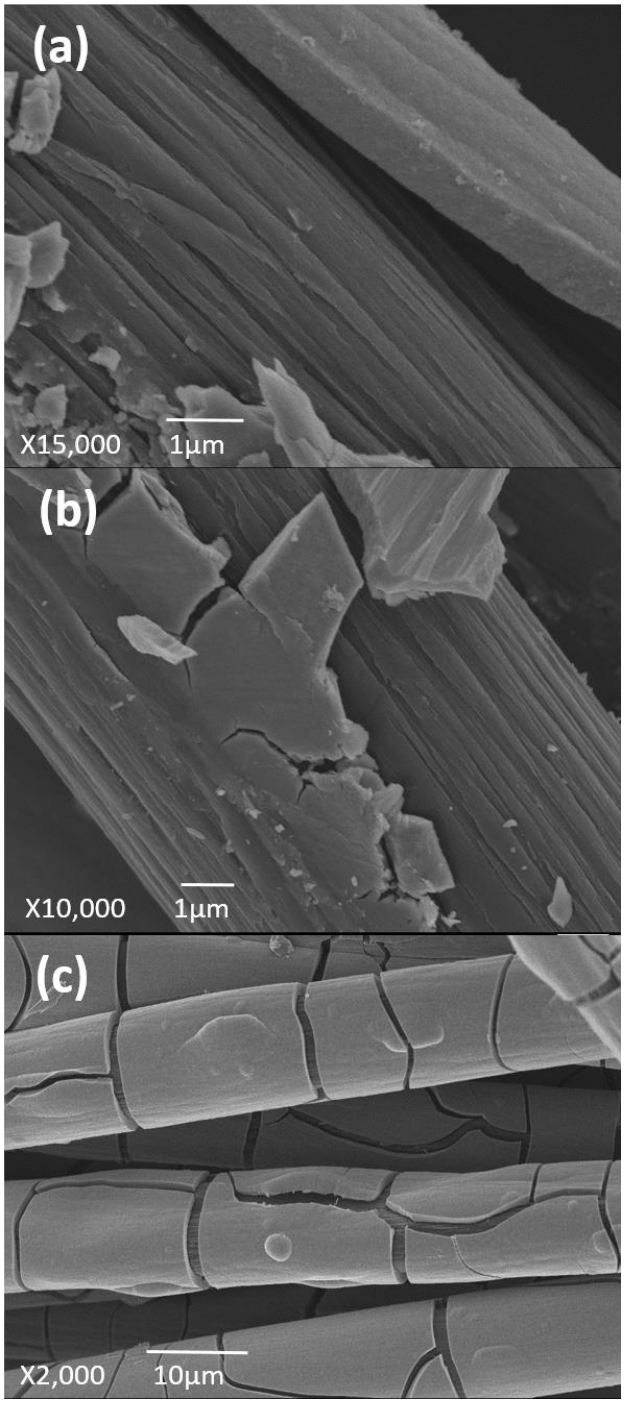

Figure 2.2 (a-c) SEM images of $FeWCo_3O_4$/CFC with different magnifications.

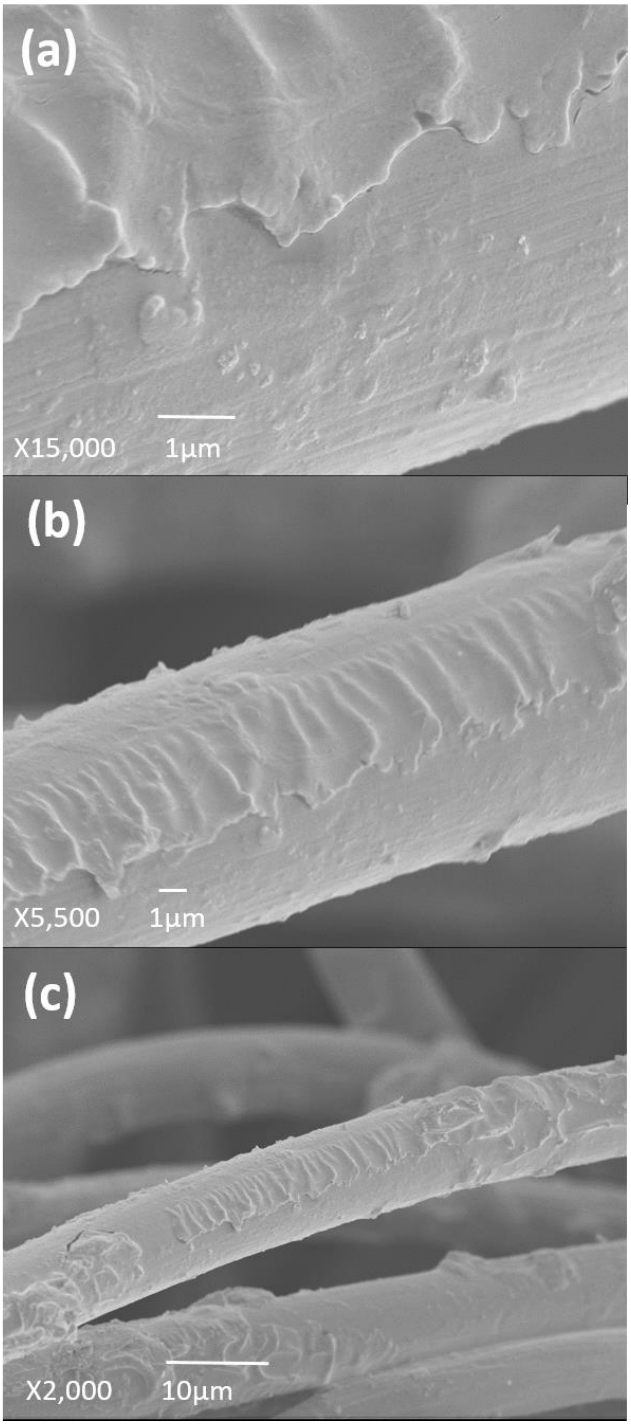

Figure 2.3 (a-c) SEM images of $FeWCo_3O_4$/PPy/CFC with different magnifications.

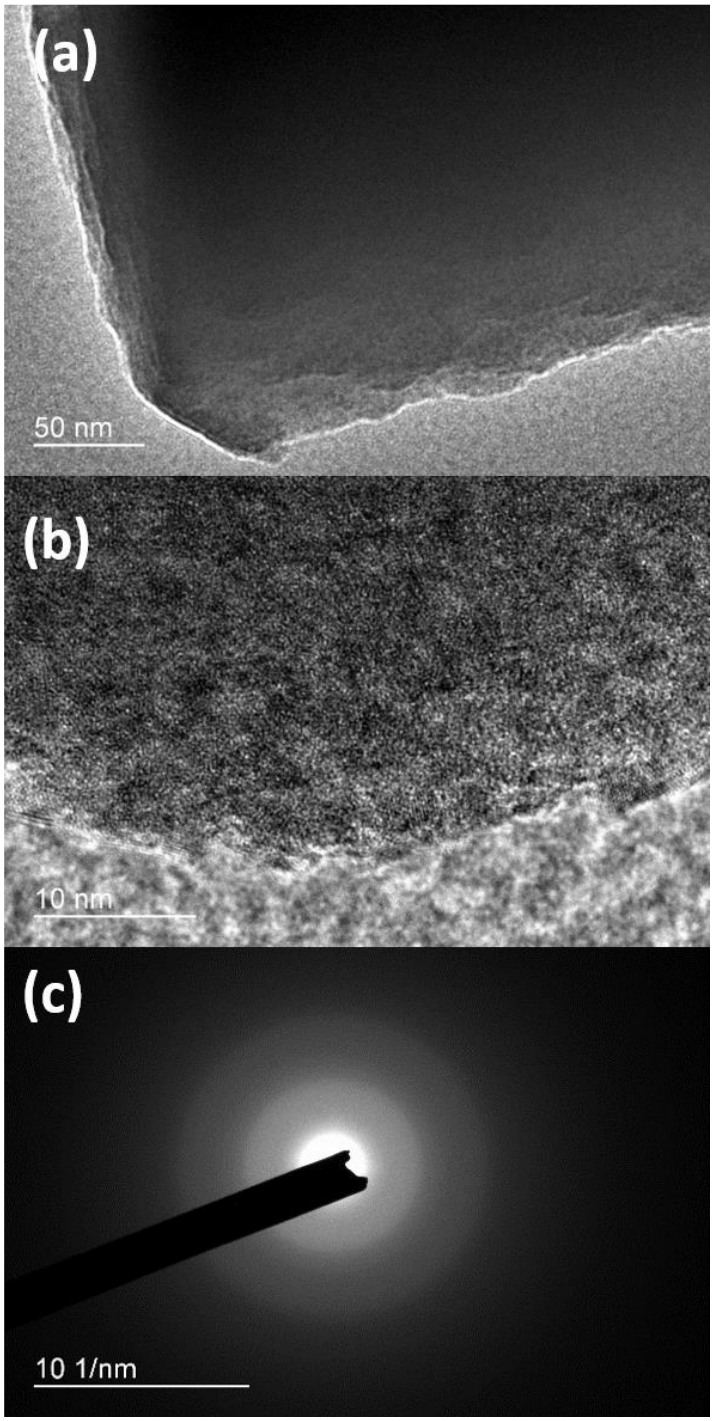

Figure 2.4 (a) TEM image, (b) HRTEM image and (c) corresponding SAED pattern of stripped $FeWCo_3O_4$ layer from $FeWCo_3O_4$/PPy/CFC.

Figure 2.2 a-c display the SEM images of $FeWCo_3O_4$ on the CFC without PPy modification under different magnifications, from which it is clear that the deposited $FeWCo_3O_4$ layer is easy to peel off. Many cracks appear on the $FeWCo_3O_4$ layer which demonstrates that this layer is fragile. The broken layers and layer cracks are probably due to the loose contact between $FeWCo_3O_4$ layer and CFC, which leads to mechanical instability of the structure of $FeWCo_3O_4$/CFC. In contrast, when the PPy modified CFC is used as substrate to deposit $FeWCo_3O_4$, the contact between $FeWCo_3O_4$ and substrate is significantly improved as shown in Figure 2.3 a-c. For the $FeWCo_3O_4$/PPy/CFC structure, no cracks can be identified from the $FeWCo_3O_4$ layer. The stable structure of $FeWCo_3O_4$/PPy/CFC provides higher amount of effective active sites, meanwhile the cracks and fallen pieces of $FeWCo_3O_4$/CFC structure will eventually cause the loss of active sites and the decrease of catalytic performance.

TEM and XRD characterization are used to identify the structure of the electrodeposited $FeWCo_3O_4$ layer. The TEM images (Figure 2.4 a) reveals the thin nanosheets coating on the CFC. No obvious lattice fringes are observed in the high-resolution TEM (Figure 2.4 b) image, and meanwhile, the

corresponding diffraction rings in SAED pattern are dispersed, indicating that the electrodeposited $FeWCo_3O_4$ is amorphous.

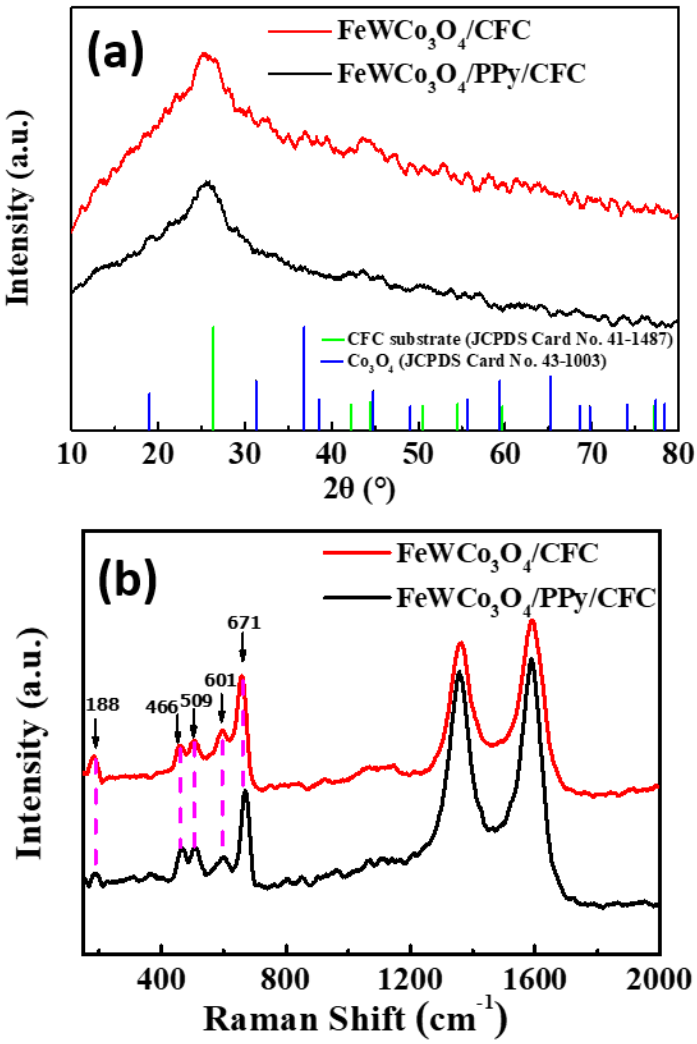

Figure 2.5 (a) XRD pattern and (b) Raman spectra of electrodeposited $FeWCo_3O_4$/PPy/CFC.

In the XRD pattern shown in Figure 2.5 a, only peaks of CFC substrate (JCPDS Card No. 41-1487) can be observed. This further confirms the amorphous structure of the $FeWCo_3O_4$ layer, in agreement with the SEAD result. To investigate the chemical composition of $FeWCo_3O_4$, Raman spectra and XPS are carried out. The Raman spectrum reveals the existence of Co_3O_4 as shown in Figure 2.5 b. The observed 188, 466, 509, 601, 671 cm^{-1} peaks agree well with pure spinel structure of Co_3O_4 [54]. The two peaks at 1360 and 1590 cm^{-1} belong to the CFC substrate.

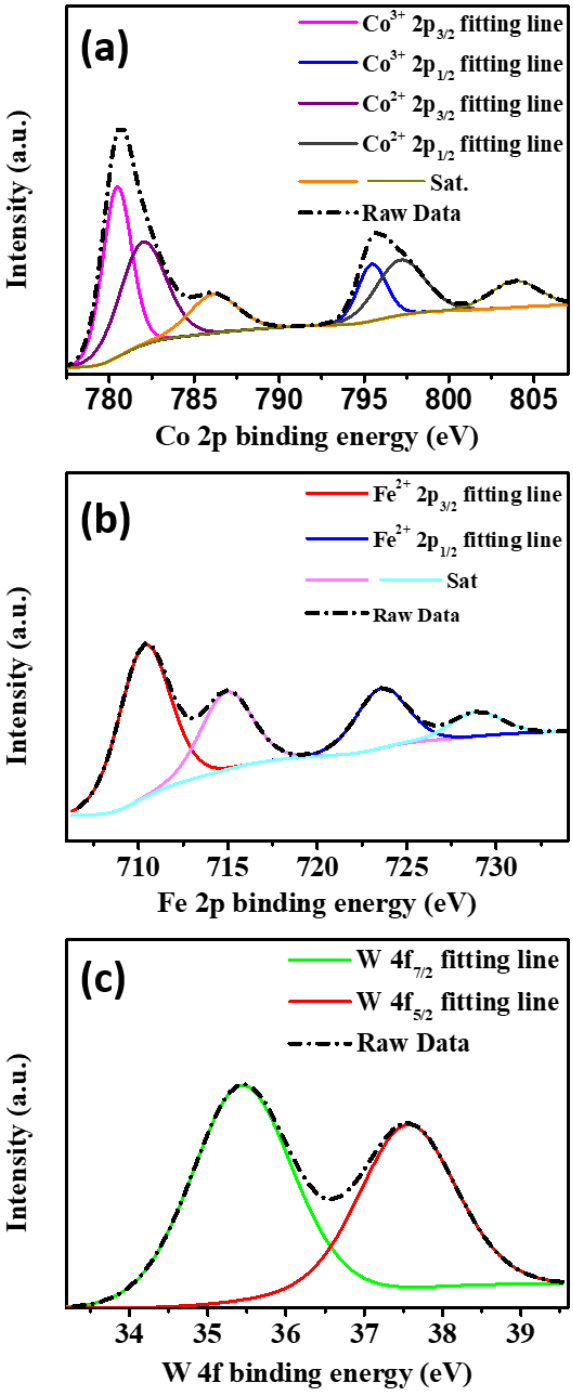

Figure 2.6 XPS of $FeWCo_3O_4$/PPy/CFC (a) Co 2p XPS, (b) Fe 2p XPS, and

(c) W 4f XPS.

XPS spectrum provides the detailed information of element states. Co_3O_4 is actually in a mixed oxidation state of Co^{2+} and Co^{3+}. As shown in Figure 2.6 a, Co consists of +2 and +3 states which is consistent with Co_3O_4 composition indicated by Raman spectra. The peaks of 780.48 eV and 782.03 eV belong to Co $2p_{3/2}$ region of Co^{3+} and Co^{2+} respectively. The corresponding satellite peak of Co $2p_{3/2}$ is observed at 786.23 eV. Peaks of Co $2p_{1/2}$ is also observed at 795.48 eV for Co^{3+} and 797.23 eV for Co^{2+}, accompanied with satellite peak (denoted as Sat.) at 803.98 eV. The peak found at 710.43 eV in Figure 2.6 b belongs to Fe^{2+} $2p_{3/2}$ with corresponding satellite peak at 715.03 eV. Peaks at 723.73 eV and 729.03 eV belong to Fe^{2+} $2p_{1/2}$ and corresponding satellite peak, respectively. It is revealed that Fe exists only at the valence state of Fe^{2+}. W 4f binding energy is measured in Figure 2.6 c. The peaks at 35.45 eV and 37.58 eV belong to W $4f_{7/2}$ and W $4f_{5/2}$ of W^{6+}, which indicate that only W^{6+} exists in the deposited $FeWCo_3O_4$. The metallic elements mainly contain Co with small amounts of Fe and W, which is further confirmed by the EDS measurement Figure 2.9.

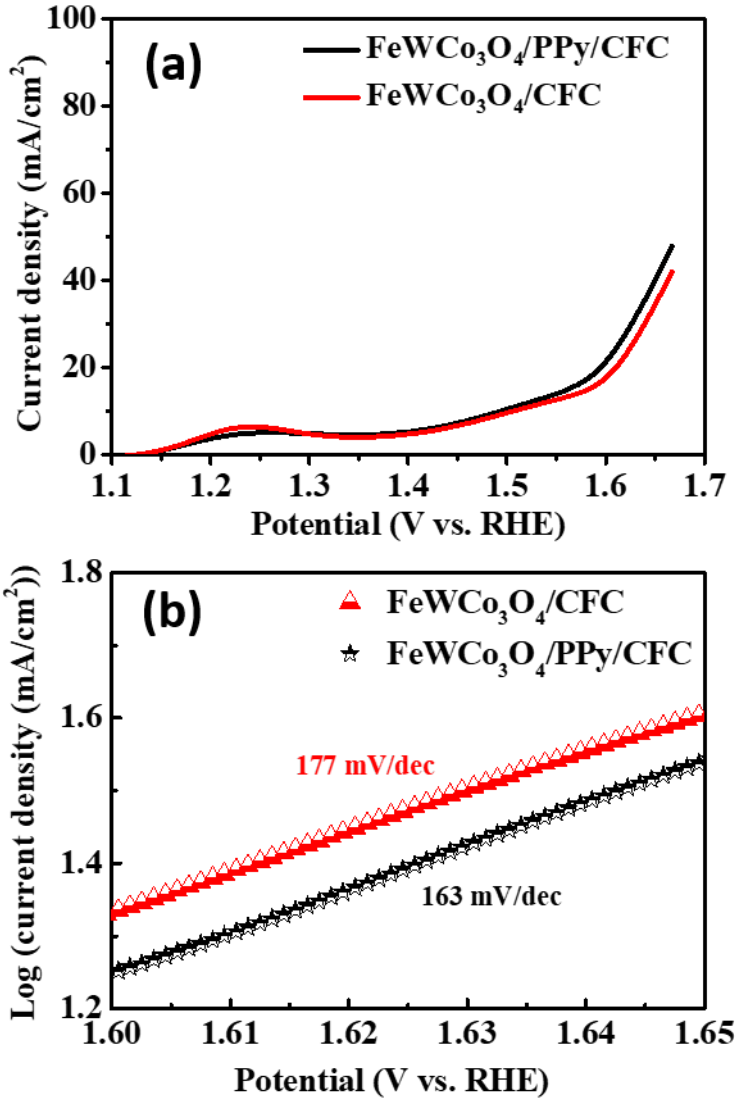

Figure 2.7 (a) Polarization curve, (b) Tafel plot of $FeWCo_3O_4$/PPy/CFC and $FeWCo_3O_4$/CFC

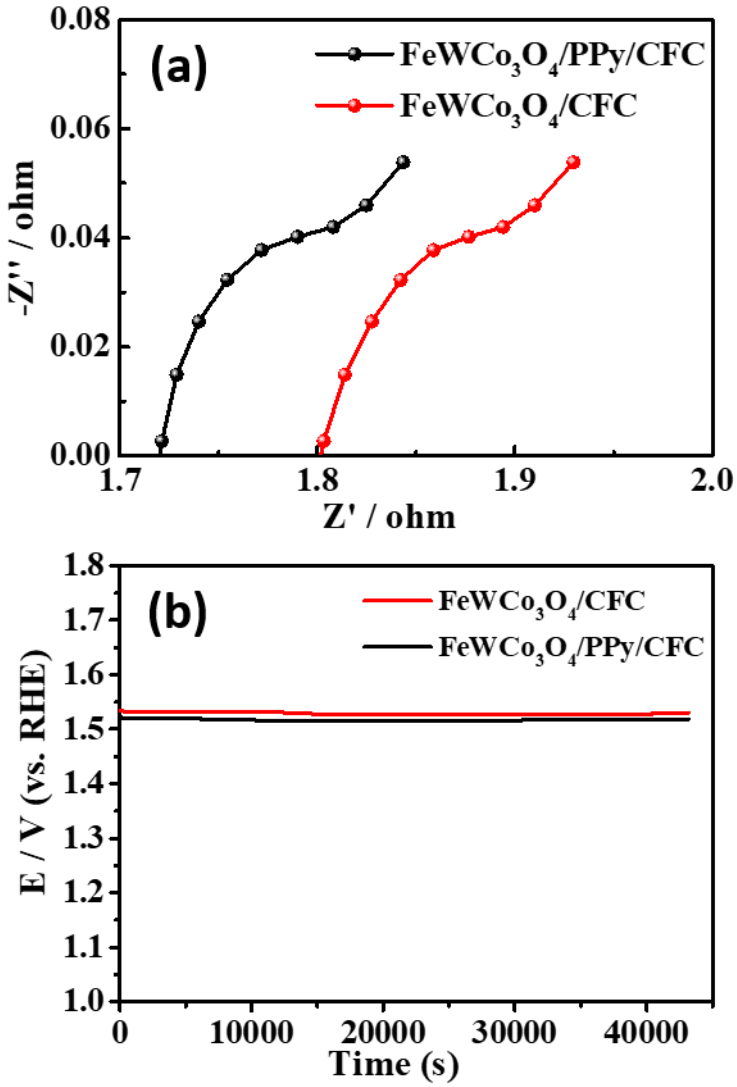

Figure 2.8 (a) EIS plot and (b) Chronopotentiometric curve of FeWCo3O4/PPy/CFC and FeWCo3O4/CFC

The OER electrocatalytic property is tested in 1.0 M KOH alkaline media at a scan rate of 2 mV s^{-1} with SCE as reference electrode and Pt plate as counter

electrode. The SCE reference electrode can be converted into revesible hydrogen electrode (RHE) reference electrode according to the following equation:

$$E(RHE)=E(SCE)+(0.059\ pH+0.242)\ V$$

The polarization curves of $FeWCo_3O_4$/PPy/CFC and $FeWCo_3O_4$/CFC are shown in Figure 2.7 a. The peaks of the polarization curves near 1.25 V (vs. RHE) may be associated with the reaction: $Co_3O_4+H_2O+OH^- \rightarrow 3CoOOH + e^-$. The formed conductive CoOOH on the surface of the electrodes is found to be active to catalyze the OER [55]. The current density of $FeWCo_3O_4$/PPy/CFC is higher than that of $FeWCo_3O_4$/CFC beyond 1.55-1.65 V (vs RHE). This can be explained by the effect of PPy on the improvement in conductivity and adhesion. PPy serves as conductive binder improves the conductivity and adhesion, resulting in increased number of active sites contacted with substrate. CV measurement indicates the existence of additional redox current from 1.35 to 1.50 V *vs.* RHE (Figure 2.11 & 2.12). Thus current density at an overpotential of 400 mV (1.63 V) is used to compare electrocatalytic performance to eliminate the influence of additional redox current. $FeWCo_3O_4$/PPy/CFC free-standing electrode is measured to reach a higher current density of 36.2 mA cm^{-2} than $FeWCo_3O_4$/CFC (30.7 mA cm^{-2})

at an overpotential of 400 mV. The Tafel slope of $FeWCo_3O_4$/PPy/CFC (163 mV dec^{-1}) is slightly lower than $FeWCo_3O_4$/CFC (177 mV dec^{-1}) (Figure 2.7 b), which can be ascribed to the enhanced electron transfer from PPy. EIS test indicates the lower resistance of $FeWCo_3O_4$/PPy/CFC than that of $FeWCo_3O_4$/CFC (Figure 2.8 a). The stability of $FeWCo_3O_4$/PPy/CFC and $FeWCo_3O_4$/CFC is tested by applying a constant current of 10 mA cm^{-2} for 12 hours (Figure 2.8 b). The catalytic performance is stable without obvious decay for 12 hours. Electrodeposition time is an important factor to influence the catalytic performance of $FeWCo_3O_4$/PPy/CFC. When the deposition time is two hours, the sample shows the best electrocatalytic performance (Figure 2.10). The difference in the electrocatalytic performance of samples deposited with different deposition time periods may result from two factors: the number of active sites and electron transportation. The sample with too short deposition time (one hour) may suffer from fewer active sites. However, the sample with too long deposition time (three hour) has thick layers which impede the electron transfer.

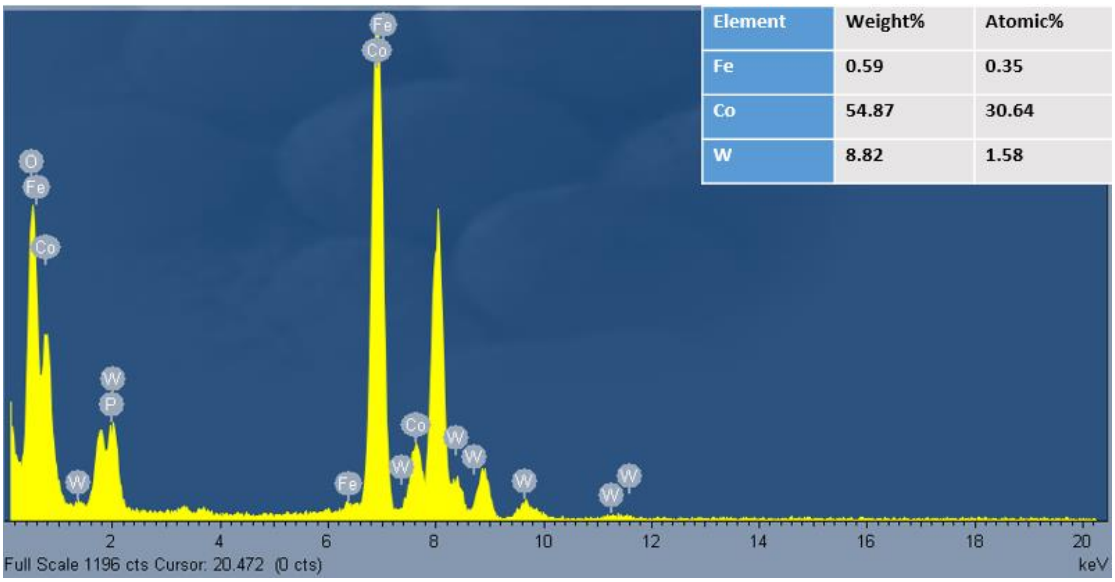

Figure 2.9 EDS measurement of $FeWCo_3O_4$

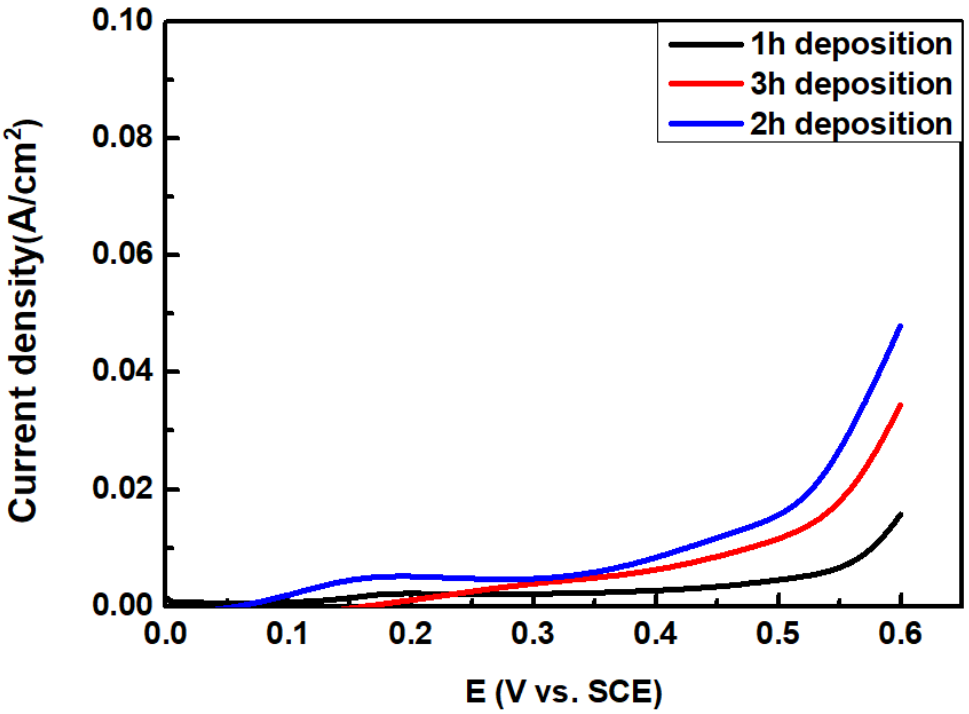

Figure 2.10 Polarization curve of $FeWCo_3O_4$/PPY/CFC electrodeposited for 1, 2, and 3 hours.

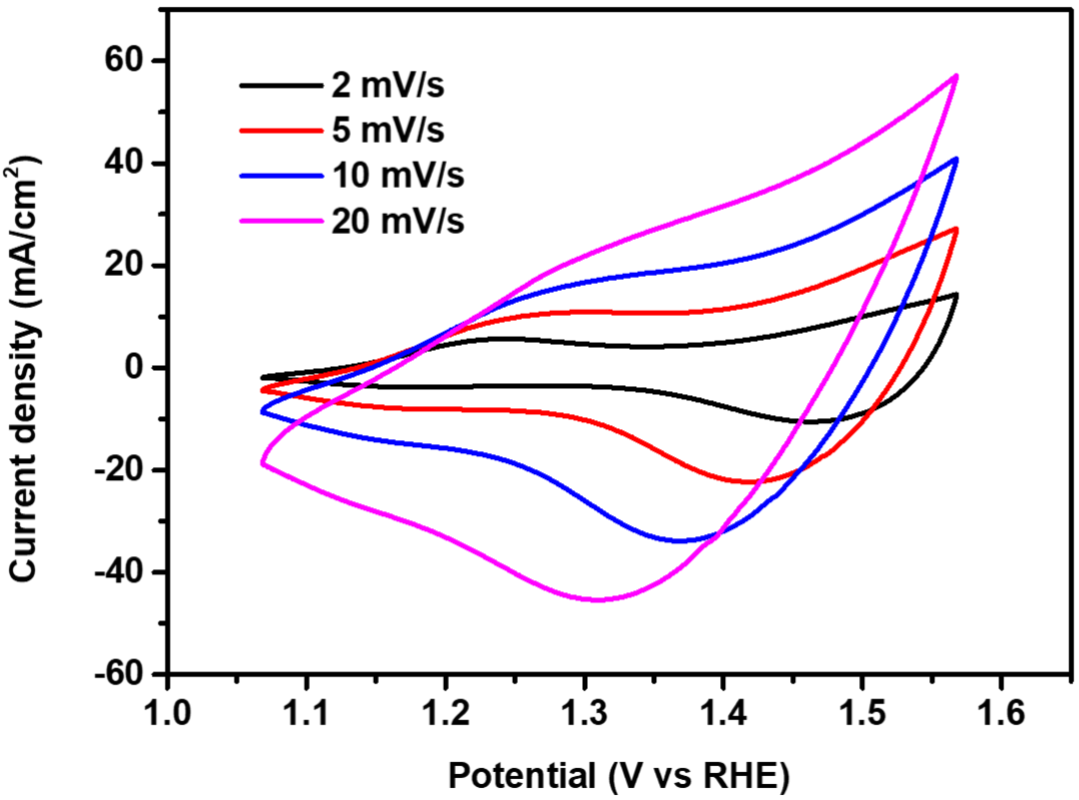

Figure 2.11 Cyclic voltammetry curve of $FeWCo_3O_4$/CFC.

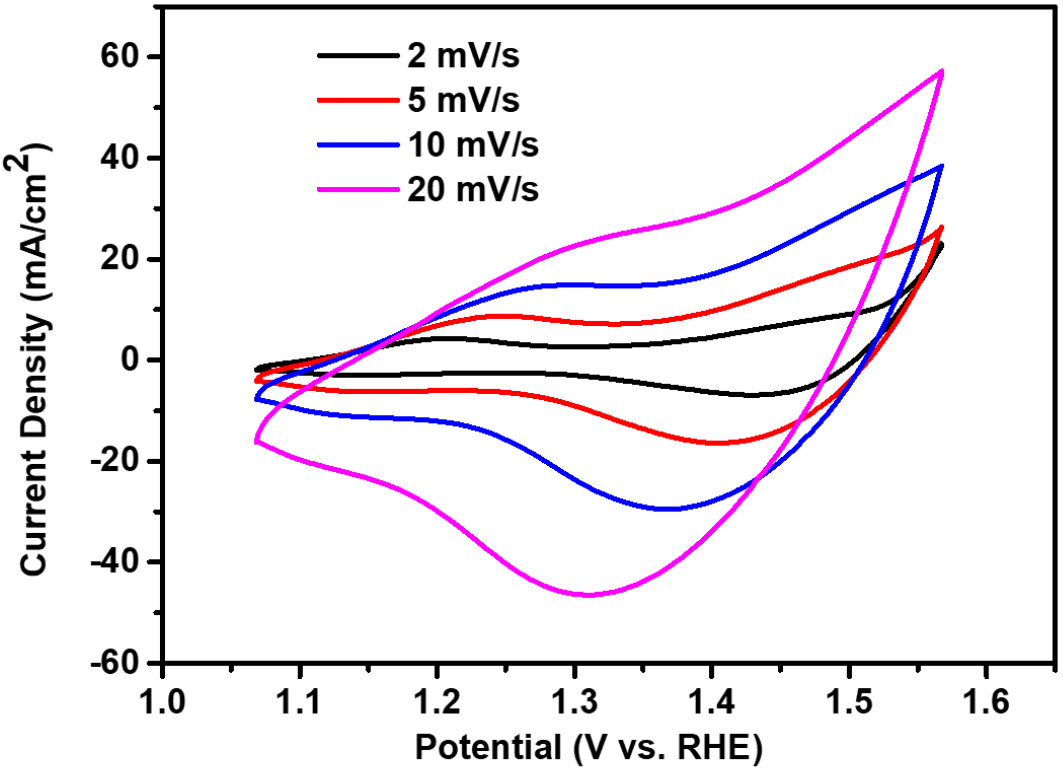

Figure 2.12 Cyclic voltammetry curve of $FeWCo_3O_4$/PPy/CFC.

2.4 Summary

By using a simple anodic electrodeposition method, amorphous Co_3O_4 co-doped with Fe, W were grown on PPy/CFC substrate. The $FeWCo_3O_4$/PPy/CFC electrode with additional PPy layer possesses better OER electrocatalytic activities than $FeWCo_3O_4$/CFC. PPy can serve as conductive binder to improve the surface contact of $FeWCo_3O_4$ active material with the substrate. Co and PPy are found to be able to form Co-N complex which can influence the adsorption and conversion process of intermedia reaction.[50] CFC is flexible and highly conductive, which is also stable at anodic condition during the deposition of $FeWCo_3O_4$. The synthesized $FeWCo_3O_4$/PPy/CFC free-standing electrode exhibits high OER catalytic performance with 36.2 mA cm^{-2} at an overpotential of 400 mV, and a Tafel slope of 163 mV dec^{-1}. This study provides new insight for design and synthesis of highly-efficient OER catalyst.

Chapter 3 One Step Synthesis of Nickel Sulfides Flakes as Efficient Electrocatalyst for Hydrogen Evolution Reaction

3.1 Introduction

The energy demand of human has been increasing with the continuous growth of world population.[56] The energy resources mainly rely on fossil fuel. The consumption of fossil fuel may lead to global warming and climate change, which has attracted more and more attention. Hydrogen as clean energy carrier has the potential to address the energy problem.[2] The combination of clean energy resource and hydrogen energy carrier provides a solution to highly efficient energy system.[3] The mass production of hydrogen from clean electricity is essential to realize hydrogen energy system.[4] Electrocatalytic hydrogen production from water involve two electrode reaction which are hydrogen evolution reaction (HER) and oxygen evolution reaction (OER). Catalysts are needed to facilitate both HER and OER. HER refers to $2H^+ + 2e^- \rightarrow H_2$. Current research efforts are focusing on developing highly efficient

catalysts, such as MoS_2[16], NiO_x[57], Ni_5P_4[58], NiS[17]. The state-of-the-art HER catalyst is Pt. However, noble metal free and earth abundant transition metal HER catalysts are demanded due to the high cost and scarcity of Pt. This study adopted a facile one-step synthesis of nickel sulfides flakes on Ni plate which show efficient HER catalytic performance. Only 112mV overpotential is needed to reach 10 mA cm^{-2} HER current density. The nickel sulfides are identified to be highly crystalline Ni_3S_2 and NiS. Nickel sulfides and Ni plate provide favorable HER catalytic property and high conductivity, which lead to overall efficient HER catalytic performance. The excellent electrochemical catalytic property is also explored by DFT calculations. The reaction intermediate adsorption energy is calculated to be highly favorable for HER energetics for (131) surface of NiS and (110) surface of Ni_3S_2.

3.2 Methods

3.2.1 Hydrothermal Method

Hydrothermal method is commonly used to synthesize nanomaterials with good crystallinity. In a typical hydrothermal synthesis, precursors are dissolved in water and added into an autoclave. Then the temperature is kept within 130 to 250 ℃ for several hours and cooled down to room temperature. Nanoparticles with various structures and compositions can be formed. The advantages of hydrothermal method are considered to be simple and easy to control the structure and composition of the final product. Hydrothermal synthesis is able to get enhanced reaction kinetics when conducted with the assistance of microwave, ultrasound or other processes.

3.2.2 Fabrication of Nickel Sulfides Flakes

All chemical reagents were of analytic purity and used without further purification. Two nickel plates were washed by deionized water (DI water) for several times and dried in a 60 ℃ oven for 2 hours. 0.005 mol Thioacetamide (C_2H_5NS) were dissolved into 50 mL DI water under continuous magnetic

stirring for 12 hours. The pH value of the solution was adjusted to 6 by dropping 2 mol/L hydrochloric acid (HCl). The two washed nickel plates and solution were transferred into a 50 mL Teflon-lined stainless steel autoclave and kept at 180 ℃ for 12 hours. The autoclave was cooled down to room temperature naturally. The nickel plates were washed by DI water and ethanol several times and dried in a 60 ℃ oven for 2 hours.

3.2.3 Characterization of Nickel Sulfides Flakes

Scanning electron microscope (SEM, TM 3000, Hetachi, Janpan) and transmission electron microscope (TEM, JOEL JEM-2010, Janpan) were used for microstructure and morphology characterization. X-ray diffraction (XRD, Rigaku D/max ⅢA, Cu Kα, λ=0.15418 nm, Japan) was used for crystalline structure analysis. Raman spectrum was conducted on a HORIBA Raman spectrometer at 488 nm.

Electrochemical Measurement

Linear sweep voltammetry (LSV), cyclic voltammetry (CV), electrochemical impedance spectroscopy (EIS, 0.01-1000k Hz frequency) and chronopotentiometric tests were performed on electrochemical workstation

(Solartron Analytical 1470E). A classical three-electrode configuration was used with carbon bar as counter electrode and saturated calomel electrode (SCE) as reference electrode. The measurement was conducted in 1 mol L^{-1} KOH solution and the polarization curve was tested at a scan rate of 2 mV s^{-1}.

Theoretical Calculation Details

Density functional theory (DFT) calculations were performed using the Vienna ab initio simulation package (VASP)[59, 60] version 5.4.4. The plane-wave basis set and projector-augmented wave (PAW)[61] pseudopotentials were adopted. For the exchange and correlation functional, generalized gradient approximation (GGA) with Perdew-Burke-Ernzerhof (PBE)[62] parametrization was applied. Kinetic energy cutoff was set as 520 eV for all calculations. The convergence threshold for geometric optimization of energy and force were 1×10^{-5} eV and 0.02 eV/Å, respectively. Monkhorst-Pack sampling[63] with 9×9×1 and 11×11×11 mesh was used for slab and bulk structure calculations. For the slab model, a vacuum layer with a thickness of 12 Å was used to minimize the interaction between adjacent image cells. Hubbard U framework with Dudarev approach[64] was applied for strongly correlated electrons in first-row transition metal ion Ni (U-J=3.6 eV).

The free energy of adsorbed H on different slab surfaces were calculated using the following formula:

$$\Delta G = \Delta E_{DFT} + \Delta E_{ZPE} - T\Delta S$$

Here ΔE_{DFT}, ΔE_{ZPE} and ΔS represent adsorption energy of one H atom (calculated using DFT), change of zero point energy and entropy, respectively. T=300 K is the temperature. During zero point energy calculations, vibration energies for all degrees of freedom were considered.

3.3 Results and Discussion

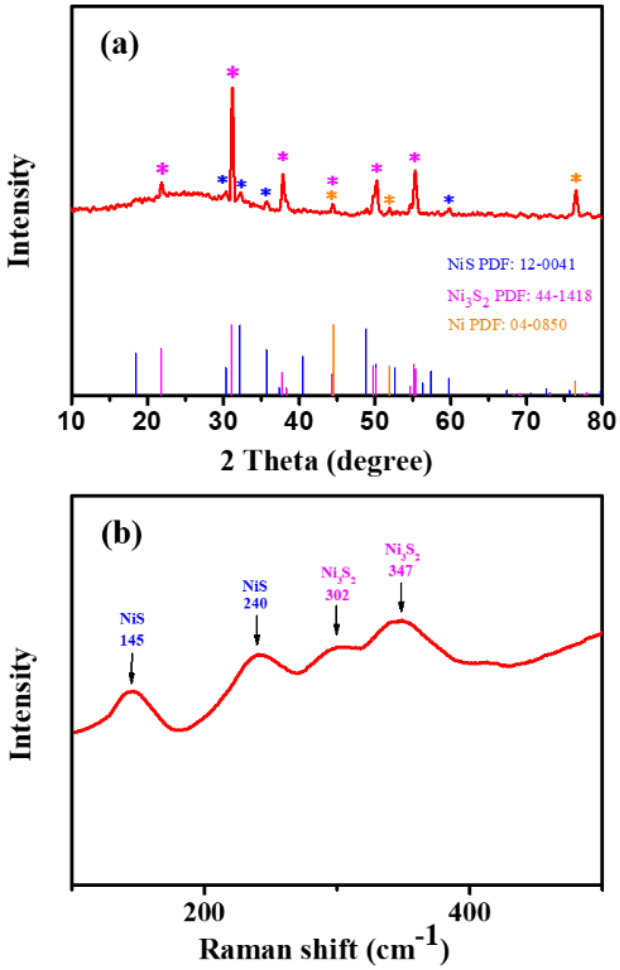

Figure 3.1 (a) XRD pattern of nickel sulfides grown on nickel plates. (b) Raman shift curve of nickel sulfides grown on nickel plates.

The content of grown nickel sulfides can be identified as a mixture of Ni_3S_2 (PDF: 44-1418) and NiS (PDF: 12-0041) as shown in Figure 3.1 a. The peaks of Ni plate substrate can also be detected. The nickel sulfides are mainly in Ni_3S_2 form, which was found to possess high intrinsic HER catalytic property.[65] The Raman shift peaks at 302 cm^{-1} and 347 cm^{-1} can be attributed to vibrational modes of rhombohedral Ni_3S_2.[66] Peaks at 145 cm^{-1} and 240 cm^{-1} can be attributed to E(5) and E(3) modes of NiS.[67]

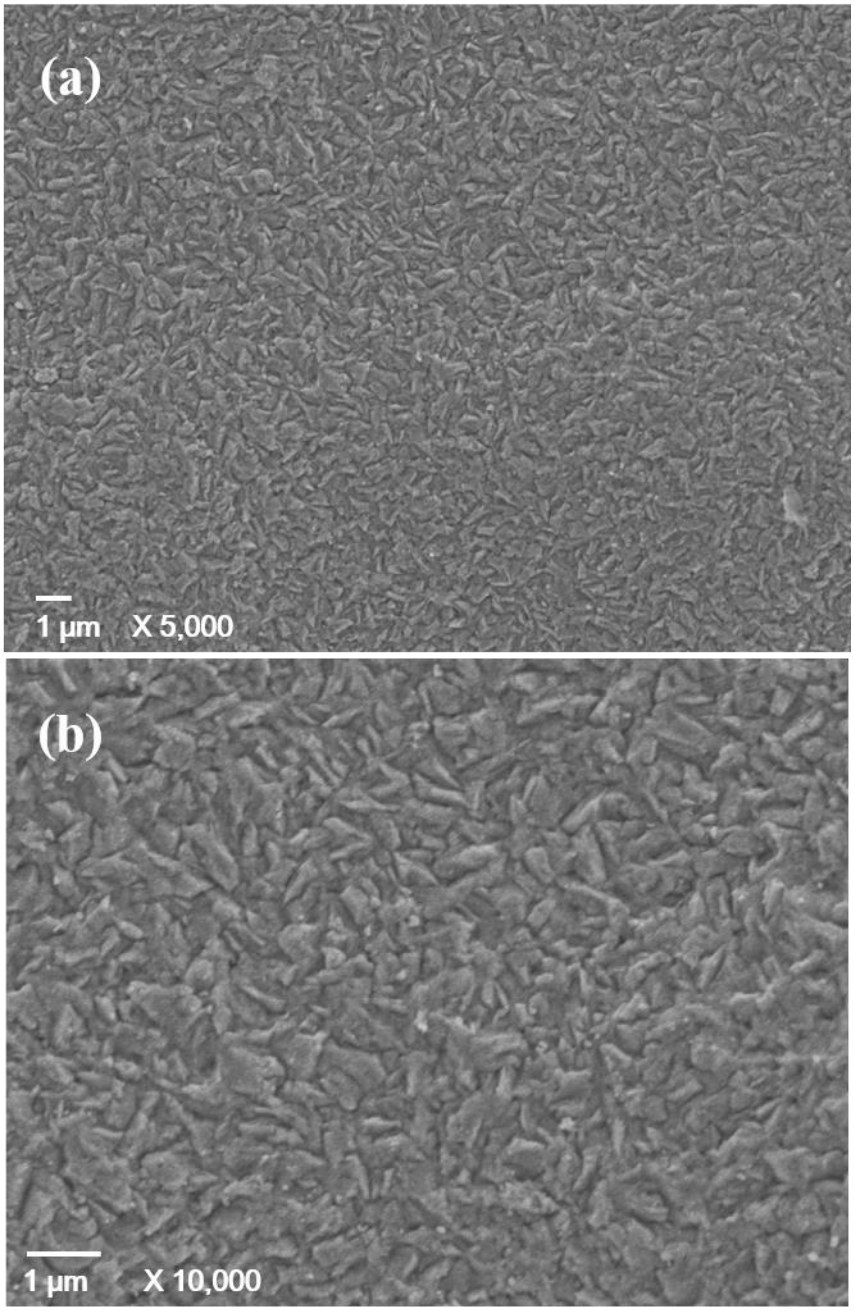

Figure 3.2 SEM image of nickel sulfides flakes at (a) low and (b) high magnifications.

SEM images show that the nickel sulfides are formed into micro-flakes, which are distributed on the surface of Ni plate substrate densely. The nickel sulfides are the active materials to catalyze HER. The Ni plate substrate were highly conductive, which enhances the electron transportation of HER at nickel sulfide surface.

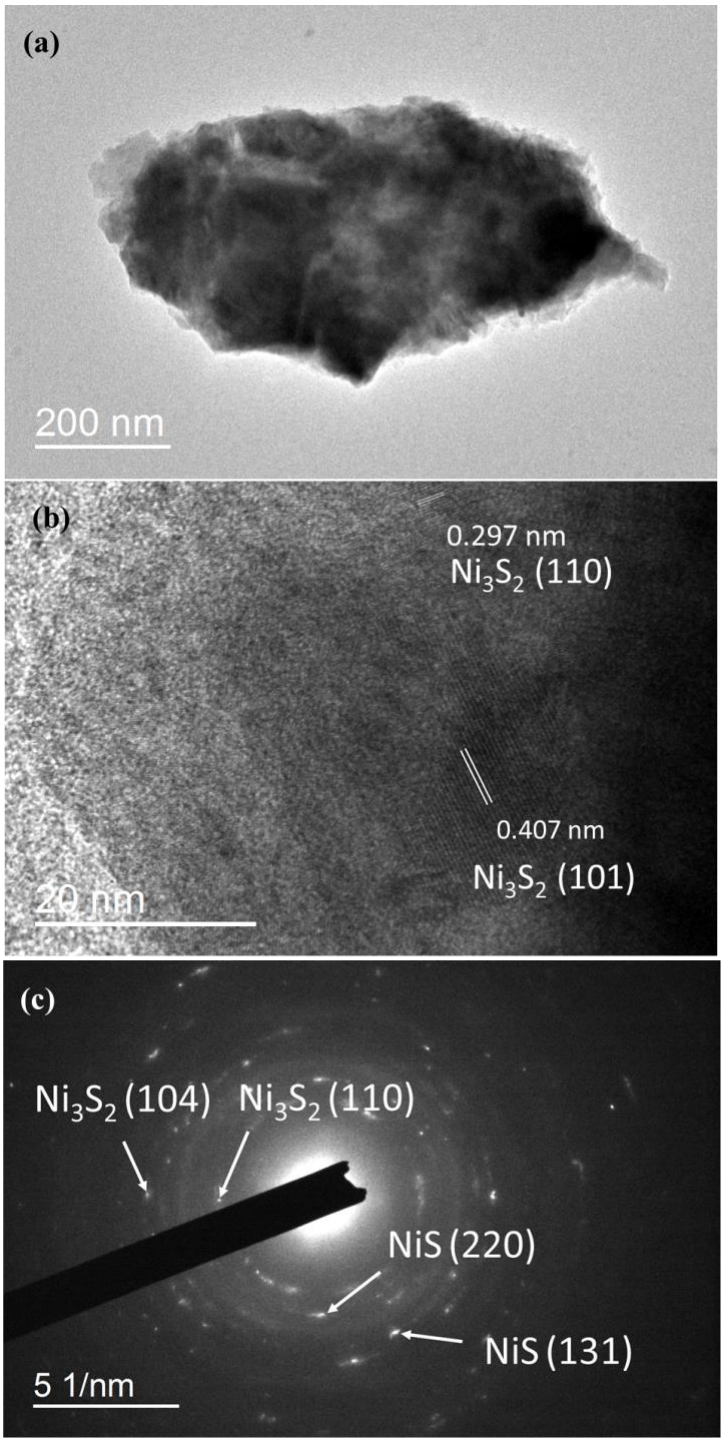

Figure 3.3 (a) TEM image, (b) high resolution TEM image, and (c) selected area electron diffraction (SAED) pattern of nickel sulfide micro-flakes.

The TEM sample was prepared by striping the nickel sulfide flakes from the nickel substrate through 30 mins ultrasonic treatment. The lattice fringes were found to belong to Ni_3S_2 as shown in Figure 3.3 b. The 0.2975 nm fringe spacing matches the (110) plane of Ni_3S_2. The 0.4071 nm fringe spacing matches the (101) plane of Ni_3S_2. SAED pattern indicates the existence of Ni_3S_2 and NiS. Bright spots can be identified to represent (110) and (104) planes of Ni_3S_2 and (220) and (131) planes of NiS, as indicated by arrows in Figure 3.3 c.

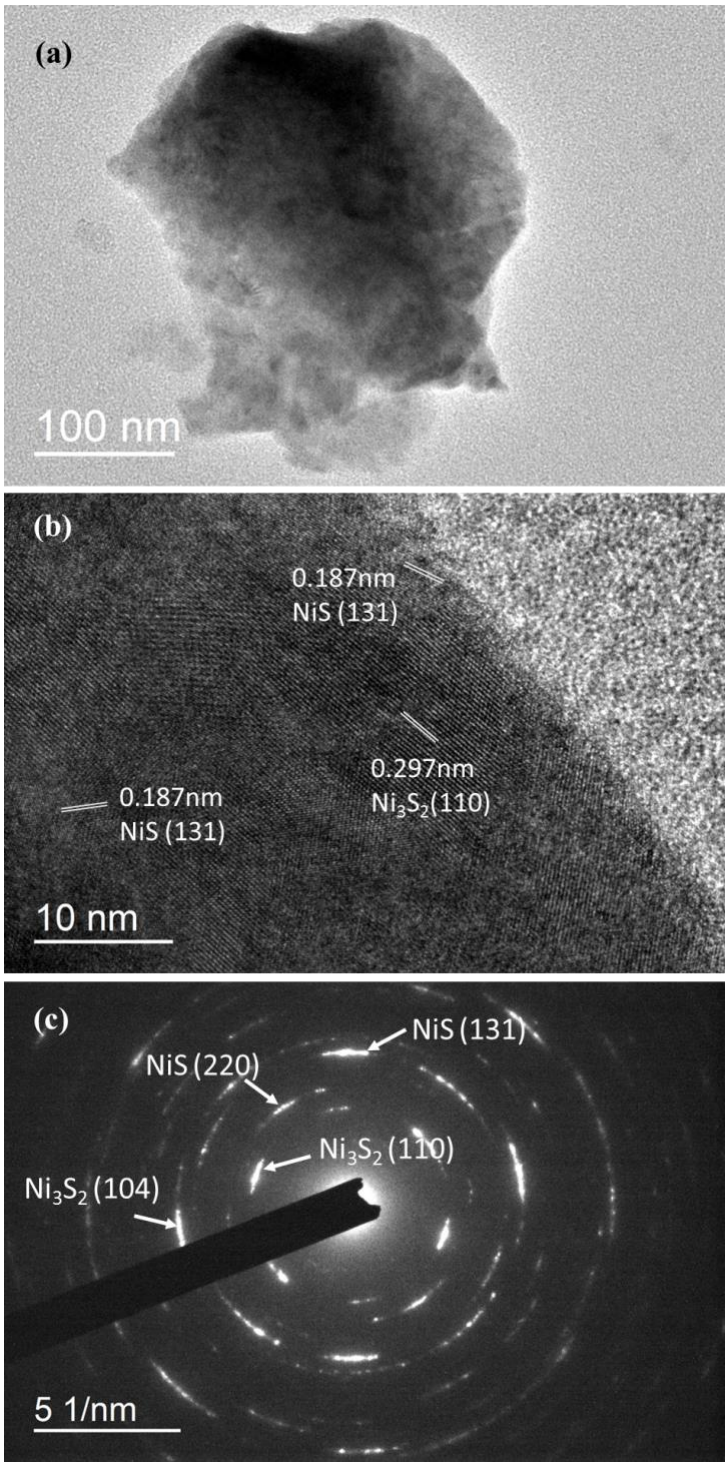

Figure 3.4 (a) TEM image, (b) high resolution TEM image, and (c) selected

area electron diffraction (SAED) pattern of nickel sulfides.

Figure 3.4 shows the TEM characterization of nickel sulfides of another sample. Small nano flake of nickel sulfide can be seen in Figure 3.4 a. High resolution TEM image shows the existence of NiS and Ni_3S_2 nanocrystals, where the *d*-spacing of Ni_3S_2 (110) planes and that of NiS (131) planes can be clearly observed in Figure 3.4 b. SAED pattern confirms the highly crystallized Ni_3S_2 and NiS nanoparticles, which favors the HER reaction intermediate energetics towards high HER electrocatalytic performance, according to DFT calculations.

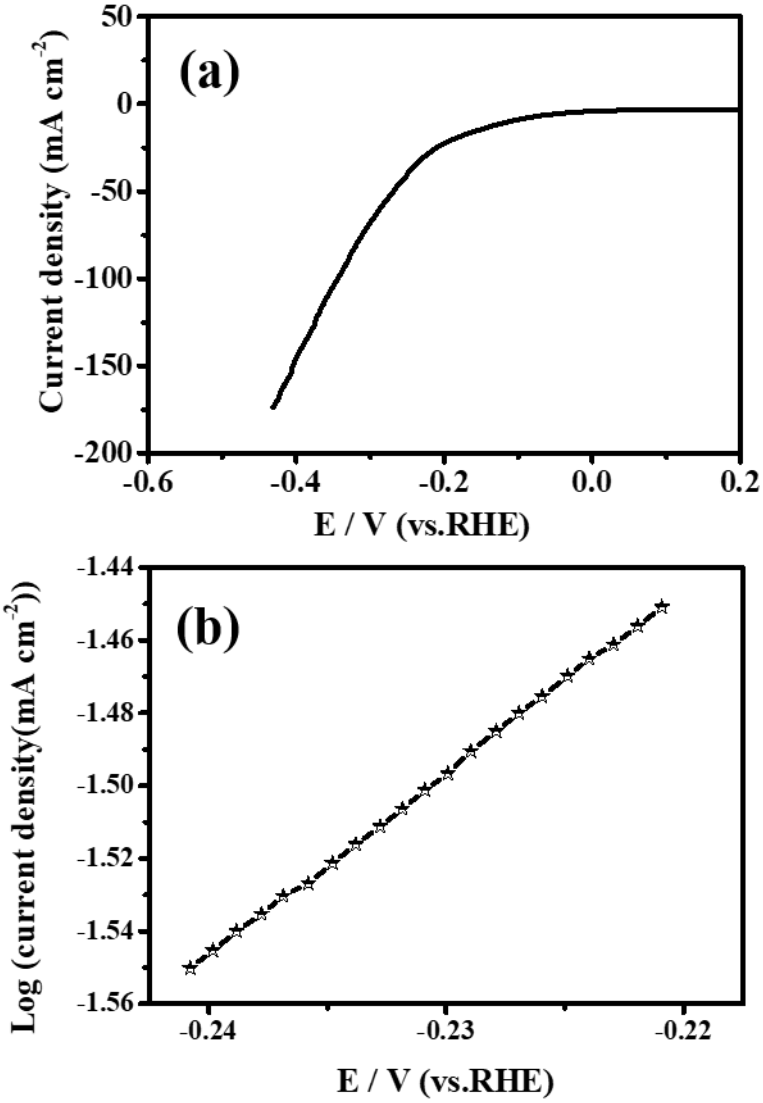

Figure 3.5 (a) Polarization curve (b) Tafel plot of nickel sulfides.

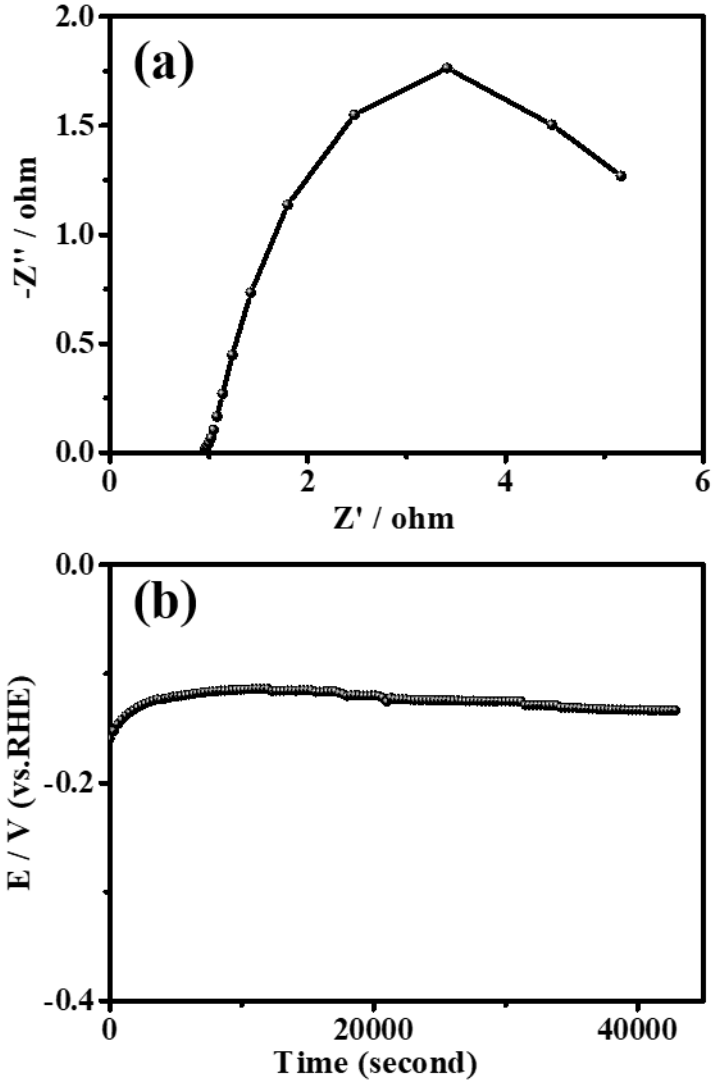

Figure 3.6 (c) EIS plot (d) Chronopotentiometric curve of nickel sulfides.

The polarization curve shows low onset potential. The ovepotential at 10 mV cm^{-2} is measured to be 112 mV without iR correction. The Tafel plot shows a relatively low Tafel slope with an approximate value of 190 mV dec^{-1}. EIS

measurement indicates that the series resistance is as low as 0.95 Ω, which may result from the highly conductive Ni_3S_2 and Ni substrate. The stability of nickel sulfides is tested under a current density of conduct 10 mA cm^{-2} for 12 hours. The chronopotentiometric curve displays overpotential drop at the first 2 hours, indicating HER catalytic performance improvement, which may due to the increasing of available active sites.

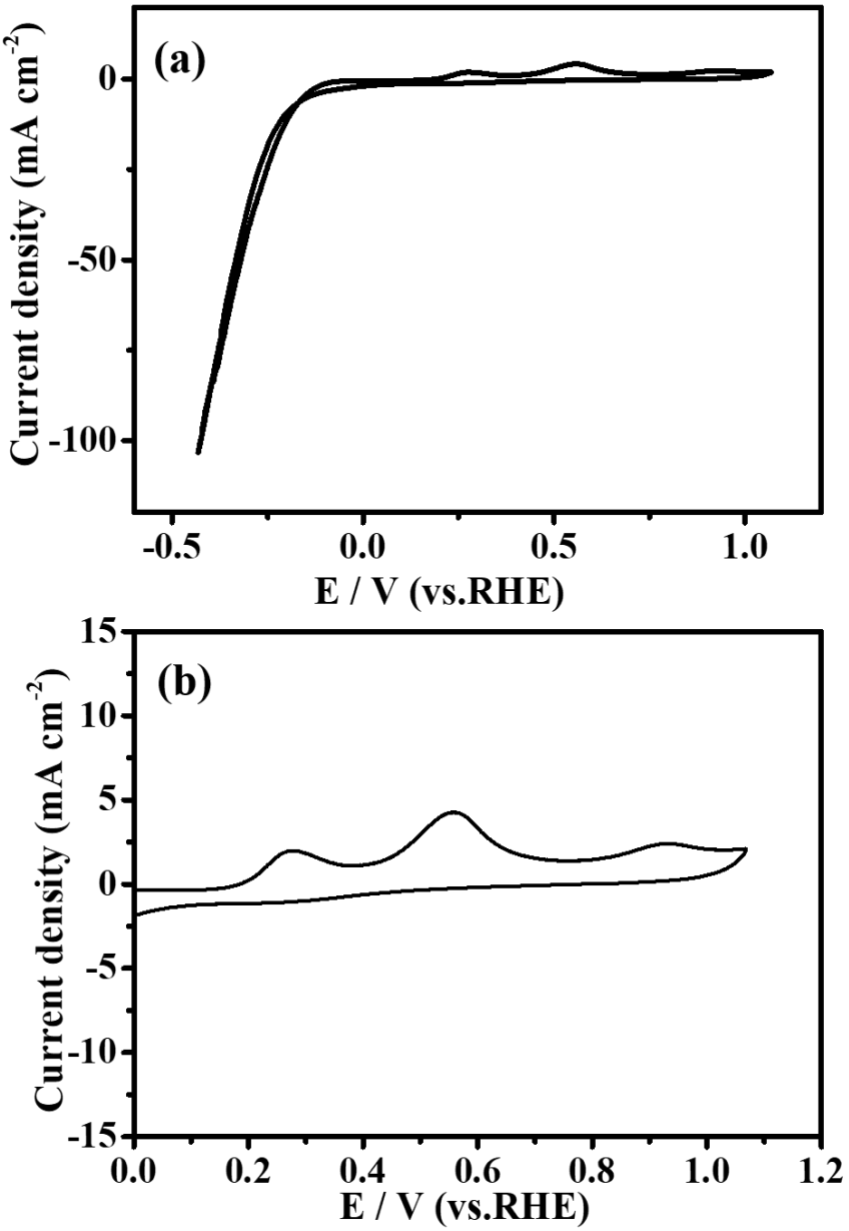

Figure 3.7 (a), (b) Cyclic voltammetry of nickel sulfides grown on Ni plate under 2 mV/s scan rate.

The electrode reaction can be investigated by analysis of cyclic voltammetry curve. The curve shows two peaks at anodic region, which are due to the oxidation of Ni_3S_2 into NiS.[68] The reactions can be written as:

$$Ni_3S_2 \rightarrow 2NiS + Ni^{2+} + 2e^- \quad (1)$$

$$NiS \rightarrow Ni^{2+} + S + 2e^- \quad (2)$$

$$NiS + 8OH^- \rightarrow Ni^{2+} + SO_4^{2-} + 4H_2O + 8e^- \quad (3)$$

The peak at 0.35 V vs RHE can be explained by reaction (1). Reactions (2) and (3) are supposed to arise simultaneously, which result in the peak at 0.55 V vs RHE.[68] The reduction curve is non zero at 0 V vs RHE as shown in Figure 3.7 b. The non-zero current is due to the reduction of surface products formed at anodic condition. The current from surface reduction is considered small when compared with the hydrogen evolution reaction current. The 2 mV/s scan rate is adopted to reduce the effect of current from non-HER current.

DFT calculations total and partial density of states (DOSs) are obtained and plotted in Figure 3.8. The main contribution of DOSs around Fermi energy level is from Ni-3d and S-3p orbitals, indicating that d-p hybridization plays a crucial role in determining the electronic properties of the system. NiS shows a semiconducting behavior with a band gap value of around 1.61 eV, as

predicted by DFT under PBE (Perdew-Burke-Ernzerhof) level. On the other hand, Ni_3S_2 bulk structure is metallic with continuous DOSs in the proximity of Fermi energy level. Thus, Ni_3S_2 generally shows higher intrinsic electrical conductivity, which can lead to fast electron transport.

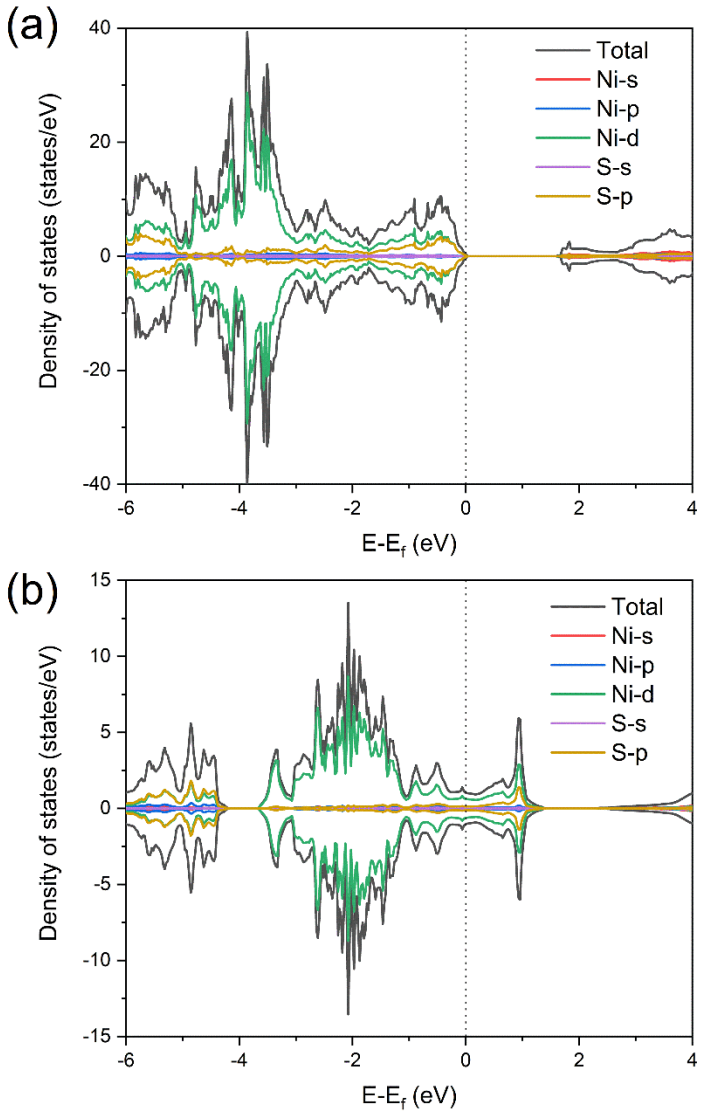

Figure 3.8 Total and partial density of states (DOSs) for (a) NiS, (b) Ni_3S_2. Dotted lines denote Fermi energy level.

To further illustrate the mechanism guiding the HER process, DFT calculations are also performed on the Gibbs free energy changes. In theory, HER can be identified as a two-step process with an initial state $H^+ + e^-$, an intermediate state of adsorbed H*, and a final state of $1/2H_2$ product.[69] ΔG of the adsorbed H* in the intermediate state should be approximately zero for an ideal HER catalyst, since $\Delta G \approx 0$ can lead to energetically favorable electron transfer and hydrogen release.[70] Predicted by DFT calculations, ΔG values with (131) surface of NiS and (110) surface of Ni_3S_2 as catalysts are 0.10 eV and -1.13 eV, respectively. The low absolute value of ΔG for (131) surface of NiS can result in fast hydrogen adsorption and desorption, leading to good HER performance.

3.4 Summary

Efficient hydrogen evolution reaction catalyst NiS_x/Ni is synthesized via a simple one-step hydrothermal method. The NiS_x flakes are identified to consist of nanocrystalline Ni_3S_2 and NiS. The overpotential for HER catalytic activity is 112 mV to reach 10 mA cm^{-2} current density with a small Tafel slope. The resistance of NiS_x/Ni is as low as 0.95 Ω and is stable to conducting 10 mA cm^{-2} current density for 12 hours. The good HER catalytic property of NiS_x/Ni is due to the highly conductive metallic Ni_3S_2 nanocrystals and the highly favorable HER energetics of the (131)-oriented NiS nanocrystals.

Chapter 4 Conclusion and Outlook

4.1 Conclusion

The fabricated PPy enhanced Fe, W co-doped Co_3O_4 free-standing electrode shows good OER electrocatalytic performance. The nickel sulfides grown on Ni metal through hydrothermal method possess favorable HER electrocatalytic performance. The research effort is mainly focused on increasing the active site availability and enhancing the reaction energetics. The design of the structure of electrode is also important. The doping of Fe and W promotes high efficiency of local adsorption environment. PPy provides obvious enhancement of the electrocatalytic performance. CFC substrate is considered to function as a stable conductive substrate with relatively high specific surface area. Anodic electrodeposition is used to achieve uniformly grown amorphous cobalt oxide. Hydrothermal method is shown to be able to grow nickel sulfide nanocrystals on the nickel plate substrate. Nickel sulfides synthesized contain

mainly NiS and Ni_3S_2 nanocrystals. The DFT calculations help disclose the origin of the good electrocatalytic performance of nickel sulfides.

4.2 Outlooks

The electrochemical water splitting is an important part in the promising hydrogen energy system. Huge research effort has been put on increasing the OER and HER efficiencies. Every improvement in the catalytic performance is appreciated and meaningful to the commercial application in industry. This work is dedicated to investigating the catalyst design strategies and explore possible synthesis methods. It would be great if this work can contribute to the development of electrochemical water splitting and provide useful references for other researchers. Improvement can be investigated through tuning the composition and increasing the crystallinity of active materials. The amount of active sites may be promoted through various treatment such as annealing. There is still much room to further enhance the efficiency of catalysts to satisfy the ever increasing demand of industry applications.

Future work will focus on improvement of the synthesized electrode. For $FeWCo_3O_4$/PPy/CFC electrode, the tuning of the Fe : Co : W molar ratio will influence the surface reaction energetics, which may result in a more efficient overall water splitting performance. The tuning of molar ratio is possible to conduct by changing the concentration of the deposition solution. The improvement of nickel sulfides electrode can be explored through two approaches in the future. One approach is to change the morphology of flakes into nanostructures to increase available active sites. The other approach is to increase the crystallinity of nickel sulfides to improve the conductivity and surface energetics.

References

1. Lee, R., *The Outlook for Population Growth.* Science, 2011. **333**(6042): p. 569-573.

2. Chu, S. and A. Majumdar, *Opportunities and challenges for a sustainable energy future.* nature, 2012. **488**(7411): p. 294-303.

3. Turner, J.A., *Sustainable Hydrogen Production.* Science, 2004. **305**(5686): p. 972-974.

4. Zou, X. and Y. Zhang, *Noble metal-free hydrogen evolution catalysts for water splitting.* Chem Soc Rev, 2015. **44**(15): p. 5148-80.

5. Seh, Z.W., et al., *Combining theory and experiment in electrocatalysis: Insights into materials design.* Science, 2017. **355**(6321).

6. Pi, Y., et al., *Ultrathin Laminar Ir Superstructure as Highly Efficient Oxygen Evolution Electrocatalyst in Broad pH Range.* Nano Letters, 2016. **16**(7): p. 4424-4430.

7. Gorlin, M., et al., *Oxygen Evolution Reaction Dynamics, Faradaic Charge Efficiency, and the Active Metal Redox States of Ni-Fe Oxide Water Splitting Electrocatalysts.* J Am Chem Soc, 2016. **138**(17): p. 5603-14.

8. Rosen, J., G.S. Hutchings, and F. Jiao, *Ordered mesoporous cobalt oxide as highly efficient oxygen evolution catalyst.* J Am Chem Soc, 2013. **135**(11): p. 4516-21.

9. Gong, M., et al., *An advanced Ni-Fe layered double hydroxide electrocatalyst for water oxidation.* J Am Chem Soc, 2013. **135**(23): p. 8452-5.

10. Jiang, N., et al., *Electrodeposited cobalt-phosphorous-derived films as competent bifunctional catalysts for overall water splitting.* Angew Chem Int Ed Engl, 2015. **54**(21): p. 6251-4.

11. Ma, T.Y., et al., *Graphitic carbon nitride nanosheet-carbon nanotube three-dimensional porous composites as high-performance oxygen evolution electrocatalysts.* Angew Chem Int Ed Engl, 2014. **53**(28): p. 7281-5.

12. Ma, W., et al., *A superlattice of alternately stacked Ni–Fe hydroxide nanosheets and graphene for efficient splitting of water.* ACS nano, 2015. **9**(2): p. 1977-1984.

13. Wang, A.-L., H. Xu, and G.-R. Li, *NiCoFe Layered Triple Hydroxides with Porous Structures as High-Performance Electrocatalysts for Overall Water Splitting.* ACS Energy Letters, 2016. **1**(2): p. 445-453.

14. Zhang, B., et al., *Homogeneously dispersed multimetal oxygen-evolving catalysts.* Science, 2016. **352**(6283): p. 333-337.

15. Lee, J.-H., D. O'Hare, and D.-Y. Jung, *Topochemical Oxidation of Transition Metals in Layered Double Hydroxides by Anthraquinone-2-sulfonate.* Bulletin of the Korean Chemical Society, 2012. **33**(2): p. 725-727.

16. Li, Y., et al., *MoS2 nanoparticles grown on graphene: an advanced catalyst for the hydrogen evolution reaction.* J Am Chem Soc, 2011. **133**(19): p. 7296-9.

17. Zhu, W., et al., *Nickel sulfide microsphere film on Ni foam as an efficient bifunctional electrocatalyst for overall water splitting.* Chem Commun (Camb), 2016. **52**(7): p. 1486-9.

18. Sun, C., et al., *Metal–organic framework derived CoSe2 nanoparticles anchored on carbon fibers as bifunctional electrocatalysts for efficient overall water splitting.* Nano Research, 2016. **9**(8): p. 2234-2243.

19. Li, Y., et al., *3D Self-Supported Fe-Doped Ni2P Nanosheet Arrays as Bifunctional Catalysts for Overall Water Splitting.* Advanced Functional Materials, 2017. **27**(37): p. 1702513.

20. Xiong, J., et al., *Salt-templated synthesis of defect-rich MoN nanosheets for boosted hydrogen evolution reaction.* Journal of Materials Chemistry A, 2017. **5**(46): p. 24193-24198.

21. Zhao, S., et al., *Ultrathin metal–organic framework nanosheets for electrocatalytic oxygen evolution.* Nature Energy, 2016. **1**: p. 16184.

22. Zhang, B., et al., *Iron–Nickel Nitride Nanostructures in Situ Grown on Surface-Redox-Etching Nickel Foam: Efficient and Ultrasustainable Electrocatalysts for Overall Water Splitting.* Chemistry of Materials, 2016. **28**(19): p. 6934-6941.

23. Tang, D., et al., *Carbon quantum dot/NiFe layered double-hydroxide composite as a highly efficient electrocatalyst for water oxidation.* ACS Appl Mater Interfaces, 2014. **6**(10): p. 7918-25.

24. Lu, Z., et al., *Electrochemical tuning of layered lithium transition metal oxides for improvement of oxygen evolution reaction.* Nat Commun, 2014. **5**: p. 4345.

25. Zhuang, Z., W. Sheng, and Y. Yan, *Synthesis of monodispere Au@Co3O4 core-shell nanocrystals and their enhanced catalytic activity for oxygen evolution reaction.* Adv Mater, 2014. **26**(23): p. 3950-5.

26. Zhao, Y., et al., *Graphene-Co(3)O(4) nanocomposite as electrocatalyst with high performance for oxygen evolution reaction.* Sci Rep, 2015. **5**: p. 7629.

27. Song, F. and X. Hu, *Ultrathin cobalt-manganese layered double hydroxide is an efficient oxygen evolution catalyst.* J Am Chem Soc, 2014. **136**(47): p. 16481-4.

28. Jiang, N., et al., *Bifunctionality and Mechanism of Electrodeposited Nickel-Phosphorous Films for Efficient Overall Water Splitting.* ChemCatChem, 2016. **8**(1): p. 106-112.

29. He, B., et al., *Facile synthesis of Ni3S2/rGO nanosheets composite on nickel foam as efficient electrocatalyst for hydrogen evolution reaction in alkaline media.* Journal of Materials Research, 2017: p. 1-9.

30. An, Y., et al., *Constructing three-dimensional porous Ni/Ni3S2 nano-interfaces for hydrogen evolution electrocatalysis under alkaline conditions.* Dalton Trans, 2017. **46**(32): p. 10700-10706.

31. Ansovini, D., et al., *A highly active hydrogen evolution electrocatalyst based on a cobalt–nickel sulfide composite electrode.* J. Mater. Chem. A, 2016. **4**(25): p. 9744-9749.

32. Burke, M.S., et al., *Oxygen Evolution Reaction Electrocatalysis on Transition Metal Oxides and (Oxy)hydroxides: Activity Trends and Design Principles.* Chemistry of Materials, 2015. **27**(22): p. 7549-7558.

33. Rossmeisl, J., et al., *Electrolysis of water on oxide surfaces.* Journal of Electroanalytical Chemistry, 2007. **607**(1-2): p. 83-89.

34. Hinnemann, B., et al., *Biomimetic Hydrogen Evolution: MoS2 Nanoparticles as Catalyst for Hydrogen Evolution.* Journal of the American Chemical Society, 2005. **127**(15): p. 5308-5309.

35. Koper, M.T.M., *Theory of multiple proton–electron transfer reactions and its implications for electrocatalysis.* Chemical Science, 2013. **4**(7): p. 2710.

36. Walter, M.G., et al., *Solar water splitting cells.* Chemical reviews, 2010. **110**(11): p. 6446-6473.

37. Dresselhaus, M. and I. Thomas, *Alternative energy technologies.* Nature, 2001. **414**(6861): p. 332-337.

38. Pletcher, D. and X. Li, *Prospects for alkaline zero gap water electrolysers for hydrogen production.* international journal of hydrogen energy, 2011. **36**(23): p. 15089-15104.

39. Reier, T., M. Oezaslan, and P. Strasser, *Electrocatalytic oxygen evolution reaction (OER) on Ru, Ir, and Pt catalysts: a comparative study of nanoparticles and bulk materials.* Acs Catalysis, 2012. **2**(8): p. 1765-1772.

40. Maiyalagan, T., et al., *Spinel-type lithium cobalt oxide as a bifunctional electrocatalyst for the oxygen evolution and oxygen reduction reactions.* Nat Commun, 2014. **5**: p. 3949.

41. Liu, Y.-C., J.A. Koza, and J.A. Switzer, *Conversion of electrodeposited Co(OH)2 to CoOOH and Co3O4, and comparison of their catalytic activity for the oxygen evolution reaction.* Electrochimica Acta, 2014. **140**: p. 359-365.

42. Zhou, Y., et al., *Ordered Mesoporous Carbon/MoO2 Nanocomposites as Stable Supercapacitor Electrodes.* ECS Electrochemistry Letters, 2012. **1**(1): p. A17-A20.

43. Gong, M. and H. Dai, *A mini review of NiFe-based materials as highly active oxygen evolution reaction electrocatalysts.* Nano Research, 2014. **8**(1): p. 23-39.

44. Huang, J., et al., *CoOOH Nanosheets with High Mass Activity for Water Oxidation.* Angew Chem Int Ed Engl, 2015. **54**(30): p. 8722-7.

45. Han, X., et al., *Ultrasensitive Iron-Triggered Nanosized Fe-CoOOH Integrated with Graphene for Highly Efficient Oxygen Evolution.* Advanced Energy Materials, 2017: p. 1602148.

46. Shang, C., et al., *Electrospun Nitrogen-Doped Carbon Nanofibers Encapsulating Cobalt Nanoparticles as Efficient Oxygen Reduction Reaction Catalysts.* ChemElectroChem, 2016. **3**(9): p. 1437-1445.

47. Liu, Y., et al., *Conformal Coating of Heterogeneous CoO/Co Nanocomposites on Carbon Nanotubes as Efficient Bifunctional Electrocatalyst for Li-Air Batteries.* Electrochimica Acta, 2016. **219**: p. 560-567.

48. Unni, S.M., et al., *High Pt Utilization Electrodes for Polymer Electrolyte Membrane Fuel Cells by Dispersing Pt Particles Formed by a*

Preprecipitation Method on Carbon "Polished" with Polypyrrole. The Journal of Physical Chemistry C, 2010. **114**(34): p. 14654-14661.

49. Bashyam, R. and P. Zelenay, *A class of non-precious metal composite catalysts for fuel cells.* Nature, 2006. **443**(7107): p. 63-6.

50. Olson, T.S., et al., *Anion-Exchange Membrane Fuel Cells: Dual-Site Mechanism of Oxygen Reduction Reaction in Alkaline Media on Cobalt−Polypyrrole Electrocatalysts.* The Journal of Physical Chemistry C, 2010. **114**(11): p. 5049-5059.

51. Koza, J.A., et al., *Electrodeposition of Crystalline Co3O4—A Catalyst for the Oxygen Evolution Reaction.* Chemistry of Materials, 2012. **24**(18): p. 3567-3573.

52. Casella, I.G. and D.A. Di Fonzo, *Anodic electrodeposition of cobalt oxides from an alkaline bath containing Co-gluconate complexes on glassy carbon. An electroanalytical investigation.* Electrochimica Acta, 2011. **56**(22): p. 7536-7540.

53. Donten, M., H. Cesiulis, and Z. Stojek, *Electrodeposition and properties of Ni ‐ W, Fe ‐ W and Fe ‐ Ni ‐ W amorphous alloys. A comparative study.* Electrochimica Acta, 2000. **45**(20): p. 3389-3396.

54. Diallo, A., et al., *Green synthesis of Co3O4nanoparticles viaAspalathus linearis: Physical properties.* Green Chemistry Letters and Reviews, 2015. **8**(3-4): p. 30-36.

55. Wang, H.Y., et al., *In Operando Identification of Geometrical-Site-Dependent Water Oxidation Activity of Spinel Co3O4.* J Am Chem Soc, 2016. **138**(1): p. 36-9.

56. Lee, R., *The outlook for population growth.* Science, 2011. **333**(6042).

57. Yu, X., et al., *Nickel-based thin film on multiwalled carbon nanotubes as an efficient bifunctional electrocatalyst for water splitting.* ACS Appl Mater Interfaces, 2014. **6**(17): p. 15395-402.

58. Ledendecker, M., et al., *The synthesis of nanostructured Ni5 P4 films and their use as a non-noble bifunctional electrocatalyst for full water splitting.* Angew Chem Int Ed Engl, 2015. **54**(42): p. 12361-5.

59. Kresse, G. and J. Furthmuller, *Efficient iterative schemes for ab initio total-energy calculations using a plane-wave basis set.* Phys. Rev. B, 1996. **54**(16): p. 11169-11186.

60. Kresse, G. and J. Furthmuller, *Efficiency of ab-initio total energy calculations for metals and semiconductors using a plane-wave basis set.* Comput. Mater. Sci., 1996. **6**(1): p. 15-50.

61. Blöchl, P.E., *Projector augmented-wave method.* Phys. Rev. B, 1994. **50**(24): p. 17953-17979.

62. Perdew, J.P., K. Burke, and M. Ernzerhof, *Generalized gradient approximation made simple.* Phys. Rev. Lett., 1996. **77**(18): p. 3865-3868.

63. Monkhorst, H.J. and J.D. Pack, *Special Points for Brillouin-Zone Integrations.* Phys. Rev. B, 1976. **13**(12): p. 5188-5192.

64. Dudarev, S., et al., *Electron-energy-loss spectra and the structural stability of nickel oxide: An LSDA+ U study.* Physical Review B, 1998. **57**(3): p. 1505.

65. Jiang, N., et al., *Nickel sulfides for electrocatalytic hydrogen evolution under alkaline conditions: a case study of crystalline NiS, NiS2, and Ni3S2 nanoparticles.* Catal. Sci. Technol., 2016. **6**(4): p. 1077-1084.

66. Feng, N., et al., *Growth of nanostructured nickel sulfide films on Ni foam as high-performance cathodes for lithium ion batteries.* Phys Chem Chem Phys, 2013. **15**(24): p. 9924-30.

67. Wang, J.H., et al., *Electronic and vibrational properties of nickel sulfides from first principles.* J Chem Phys, 2007. **127**(21): p. 214705.

68. Power, G.P., *The electrochemistry of the nickel sulfides—2. Ni3S2.* Electrochimica Acta, 1982. **27**(3): p. 359-364.

69. Nørskov, J.K., et al., *Trends in the exchange current for hydrogen evolution.* Journal of the Electrochemical Society, 2005. **152**(3): p. J23-J26.

70. Hinnemann, B., et al., *Biomimetic hydrogen evolution: MoS2 nanoparticles as catalyst for hydrogen evolution.* Journal of the American Chemical Society, 2005. **127**(15): p. 5308-5309.